EFFECTS OF EDGE SAFETY FACTOR ON THE TOROIDAL FLOW VELOCITY OF THE STOR-M PLASMA

A Thesis Submitted to the College of

Graduate Studies and Research

In Partial Fulfillment of the Requirements

For the Degree of Master of Science

In the Department of Physics and Engineering Physics

University of Saskatchewan

Saskatoon

By

EKOW LEWIS

PERMISSION TO USE

In presenting this thesis in partial fulfilment of the requirements for a Postgraduate degree from the University of Saskatchewan, I agree that the Libraries of this University may make it freely available for inspection. I further agree that permission for copying of this thesis in any manner, in whole or in part, for scholarly purposes may be granted by the professor or professors who supervised my thesis work or, in their absence, by the Head of the Department or the Dean of the College in which my thesis work was done. It is understood that any copying or publication or use of this thesis or parts thereof for financial gain shall not be allowed without my written permission. It is also understood that due recognition shall be given to me and to the University of Saskatchewan in any scholarly use which may be made of any material in my thesis.

Requests for permission to copy or to make other use of material in this thesis in whole or part should be addressed to:

Head of the Department of Physics and Engineering Physics

116 Science Place

University of Saskatchewan

Saskatoon, Saskatchewan, S7N 5E2

Canada

Dedicated to Paakow

ABSTRACT

The effect of changing edge safety factor on the toroidal flow of the STOR-M plasma has been investigated during the application of both resonant magnetic perturbation (RMP) and compact torus injection (CTI). The edge safety factor was varied by varying the plasma current while keeping the toroidal field constant. A Czyner-Turner spectrometer was used to collect the spectral data from which the velocity of specific impurity ions was diagnosed. Time resolved velocity measurements were inferred from the Doppler wavelength shift of the emission lines. Impurity emission lines at different ionization stages are located at different radial locations within the STOR-M plasma. Properties of these impurity ions are assumed to be closely related the hydrogen ion (main working gas) due to the strong interaction among the ion species.

Changing the edge safety factor has a similar effect on the toroidal flow of STOR-M plasma during discharges with both RMP and CTI. A velocity shear was discovered for different impurity ions. The toroidal flow is enhanced for edge ions while a reversal of flow is observed for core ions. As the edge safety factor reduces, the emission location for the core ions is located with $q = 2$ surface and RMP has a significant impact on their toroidal flow velocity. It was also observed that CT injection has a significant effect on the toroidal velocity of the core ions compared to that of the edge ions. In addition, high plasma current (low safety factor) induced large change in the toroidal flow velocity of the STOR-M plasma.

ACKNOWLEDGMENTS

It would not have been possible to complete this thesis without the help and support of the kind people around me, to only some of whom it is possible to give particular mention here. Above all, I would like to thank my supervisor, Dr. Chijin Xiao, whose contribution in stimulating suggestions and encouragement helped me to coordinate my project especially in writing this thesis. Furthermore I would like to acknowledge with much appreciation the crucial role of the director of the Plasma Physics Laboratory, Dr. Akira Hirose, who gave the permission to use all required equipment and necessary materials to complete this research. My parents, brother and sister have given me their unequivocal support throughout, as always, for which my mere expression of thanks likewise does not suffice. This thesis would not have been possible without the help, support and patience of David McColl and Debjyoti Basu, not to mention their advice and unsurpassed knowledge of the STOR-M tokamak. The good advice, support and friendship of my fellow graduate students have been invaluable on both an academic and a personal level, for which I am extremely grateful.

I would like to acknowledge the financial, academic and technical support of the University of Saskatchewan, Natural Sciences and Engineering Research Council of Canada (NSERC) and the Sylvia Fedoruk Canadian Centre for Nuclear Innovation. Last, but by no means least, I thank my friends in Ghana, Canada and elsewhere for their support and encouragement throughout.

TABLE OF CONTENTS

LIST OF TABLES

LIST OF FIGURES

LIST OF ABBREVIATIONS AND SYMBOLS

Abbreviation	Definition
AC	Alternating Current
BNC	Byonet Nut Coupling
CT	Compact Torus
DAQ	Data AQuisition
ELM	Edge Localized Mode
FB	Feedback
FWHM	Full Width at Half Maximum
FRMP	Fast Resonant Magnetic Perturbation
H-Mode	Improved Confinement Discharge
IGBT	Insulated Gate Bipolar Transistor
ITER	International Thermonuclear Experimental Reactor
JET	Joint European Torus
L-Mode	Normal Confinement Discharge
MHD	Magnetohydrodynamic
NBI	Neutral Beam Injection

NTM	Neoclassical Tearing Mode
OH	Ohmic Heating
PA	Principal Axis
PC	Principal Component
PMT	PhotoMultiplier Tube
PPL	Plasma Physics Laboratory
RF	Radio Frequency
RMP	Resonant Magnetic Perturbation
SOL	Scrape-Off Layer
SRMP	Slow Resonant Magnetic Perturbation
STOR-M	Saskatchewan Torus Modified
STOR-1M	Saskatchewan Torus-1 Modified
SXR	Soft X-Ray
TH	Turbulent Heating
VE	Vertical Equilibrium

Symbol	Definition
a	Minor radius
A	Cross-section
$\boldsymbol{B}$	Magnetic field
B_r	Radial magnetic field
B_z	Axial magnetic field
$B_\perp$	Vertical magnetic field
B_θ	Poloidal magnetic field
B_ϕ	Toroidal magnetic field
c	Speed of light
C	Capacitance
C_m	Fourier cosine coefficient
D	Deuterium
e	Elementary charge
$\boldsymbol{E}$	Electric field
f	Frequency
F	Force

h	Planck constant
I	Current
I_p	Plasma current
J	Current density
l_i	Internal inductance
$\ln \Lambda$	Coulomb logarithm
L	Inductance
L_p	Plasma inductance
m	Poloidal mode number
n	Toroidal mode number
n_e	Electron density
n_i	Ion density
N	Number of turns
p	Pressure
p_e	Electron pressure
p_i	Ion pressure
P	Heating power density

q	Safety factor
r	Radial coordinate
R	Major radius
R_p	Plasma resistance
S_m	Fourier sine coefficient
t	Time
T_e	Electron temperature
T_i	Ion temperature
T	Tritium
v	Velocity
v_e	Electron velocity
v_i	Ion velocity
V	Voltage
V_l	Loop voltage
$\parallel$	Parallel to magnetic field
$\perp$	Perpendicular to magnetic field
∇	Gradient operator

λ	Wavelength
$\Delta\lambda$	Wavelength shift
m_l	Magnetic number
d	Grating constant
μ_B	Bohr magnetron
θ	Azimuthal coordinate
ϕ	Toroidal coordinate
θ_i	Incidence angle
θ_d	Diffraction angle
ω_c	Cyclotron frequency
η	Plasma resistivity

Chapter One

Introduction

In this chapter, the need for the exploitation and development of sustainable fusion energy sources will be discussed. Focus would be on the operation of the STOR-M tokamak with a brief description of some relevant features and operation of a generic tokamak. The objective of this research will be discussed and an outline of the thesis will be given.

1.1 Background

Energy is one of the major building blocks of the modern society. The availability of an adequate and reliable supply of energy is essential for economic development. The world now faces an energy shortage, which can only be resolved by the development of new energy technologies. A feasible option is the creation of a large-scale environmentally friendly energy source such as fusion energy to be discussed in this thesis. The fusion energy source is based on nuclear fusion reaction in which two particles of smaller masses and charge come together to form a heavier particle. As a consequence of special theory of relativity, when the mass of some system reduces by an amount Δm, then an amount of energy E is released

$$E = \Delta m c^2 \tag{1.1}$$

where c is the speed of light. This is the basis on which energy is derived from nuclear reactions. The sun is the best example of a burning fusion reactor. The fusion of hydrogen is the main reaction that powers the sun.

The most tractable fusion reaction to create experimentally is between deuterium ${}_1^2D$ and tritium ${}_1^3T$. This reaction has a higher cross section at practically lower energies compared with other fusion reactions [1]. Deuterium is abundant in seawater while tritium can be breed from nuclear reactors by neutron activation of lithium. A typical reaction is

$$ {}_1^2D + {}_1^3T \rightarrow {}_2^4He(3.5\ \text{MeV}) + {}_0^1n(14.1\ \text{MeV}) \tag{1.2} $$

where ${}_2^4He$ is an α-particle and ${}_0^1n$ is an energetic neutron. The D-T reactions occur at a higher cross-section compared with other fusion reactions at the same energy, thereby making it easier to build such a reactor [2]. For a fusion power reactor, the majority of the neutron would be used to breed tritium from a lithium blanket around the fusion reactor core. The physical parameters necessary for this reaction to happen requires the charged particles to overcome the repulsion force between them. An economically viable reactor requires sufficiently high temperature and densities resulting in a state of matter known as plasma, which is a quasi-neutral gas composed of neutral and charged particles exhibiting collective behaviours. The plasma also needs a high confinement time for a practical fusion reactor [3].

There are two methods of plasma confinement in the laboratory. The first is inertial confinement fusion, which makes use of high-power pulsed lasers to compress a fusing target [4]. The second, which is the most relevant for this thesis, is magnetic confinement fusion. This scheme makes use of the Lorentz force for charged particles in magnetic fields which can trap

the charged particles perpendicular to their field direction [5]. Several magnetic field topologies have been considered, however the tokamak is the most developed and promising approach. The most stable shape for magnetically confined plasma is a donut shape (toroid). Tokamak is a Russian acronym for a phrase which means toroidal vessel with magnetic coils [6]. Figure 1.1 shows a drawing of a generic tokamak.

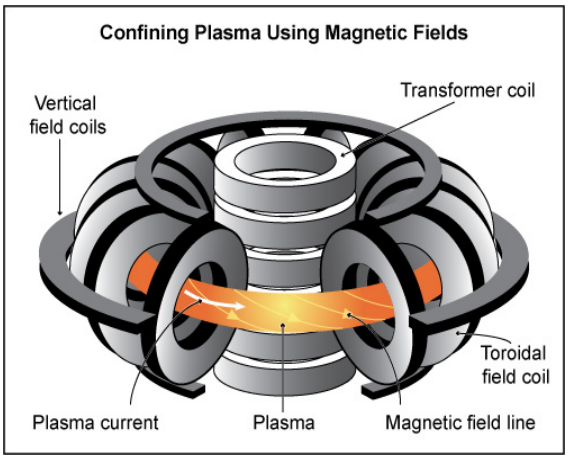

Figure 1.1: A schematic of a generic tokamak showing its main components [7]. In order to achieve stable plasma equilibrium, a helical magnetic field is needed. This is created by a combination of the externally applied toroidal (along the large circumference) field and the poloidal (along the small circumference) field generated by the plasma current.

The plasma is created in a vacuum chamber surrounded by magnetic coils which create a toroidal (along the large circumference) magnetic field. This field alone does not allow confinement of the plasma. To obtain equilibrium, in which plasma pressure is balanced by magnetic forces, it is necessary to have poloidal (along the small circumference of the cross-section of the torus) magnetic field. The electric current generated in the plasma ring produces the poloidal field. The combination of the toroidal field and poloidal field produces helical

magnetic field lines. It is this helical magnetic field that confines the plasma. It has also been found experimentally that energy confinement τ_E improves with size and scales as

$$\tau_E \propto \frac{a^{0.3} R^{1.2} {I_p}^{0.89}}{P^{0.5}} \tag{1.3}$$

where a is the mean minor radius of the plasma, R is the major radius, I_p is the plasma current and P is the heating power [8].

In order for a tokamak to be used as a reactor, additional structure modifications would be needed to convert the fusion power into electricity. The plasma would have to be surrounded by a lithium blanket to allow breeding of tritium to fuel the reactor. Also, as a measure against radiation damage and heating of the coils, a protective shield made of high thermal impedance material must be placed between the blanket and the coils. This reduces the energy flux of the neutrons that escape the outer wall of the blanket. The energy from the plasma and heat produced in the blanket would be removed by a coolant and transferred to a steam turbine engine for electricity generation. Figure 1.2 shows the schematic for a fusion power plant.

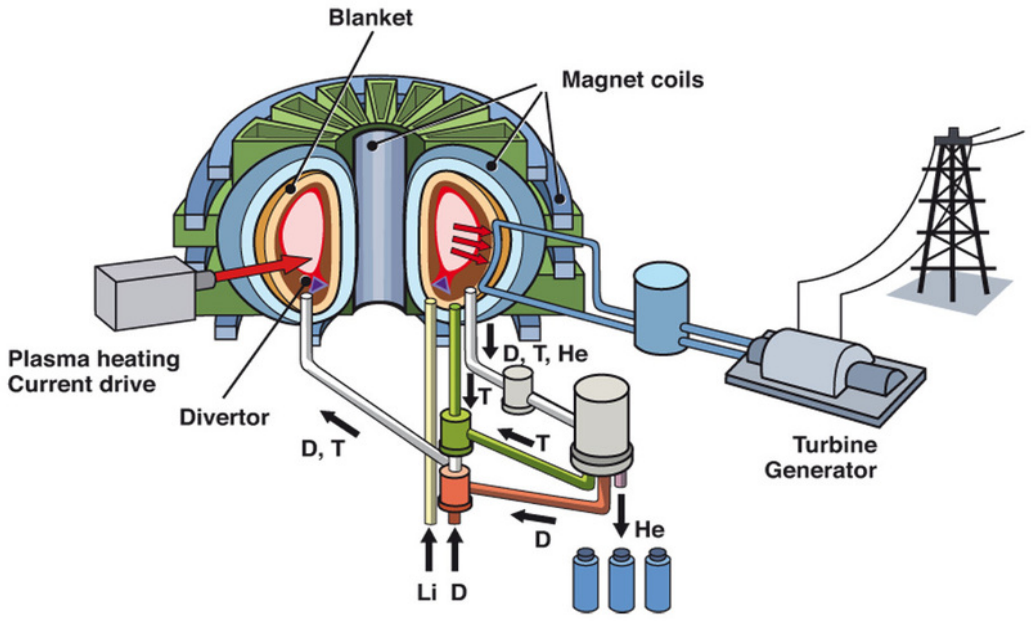

Figure 1.2: Layout of fusion power plant [9]. The blanket is enclosed in a sheath that screens the magnets, heating facilities and the other surroundings from radiations and neutrons. Lithium is embedded in the blanket which reacts with the neutron to produce tritium for fuelling the reaction

For a fusion power plant to be economically tractable, a $Q \geq 10$ is needed [10]. Q is the ratio of fusion power to input power to heat and confine the plasma. The $Q = 1$ condition represents break even, where the input power is equal to the thermonuclear power. JT60-U, a Japanese tokamak, has achieved an equivalent Q of 1.25 [11]. This record so far inspires the confidence that an efficient reactor can be built. The remainder of this thesis describes research done at an experimental magnetic confinement facility called the STOR-M tokamak at the University of Saskatchewan.

1.2 The STOR-M Tokamak

1.2.1 General Description

STOR-M is a small iron core research tokamak located in the Plasma Physics Laboratory (PPL) at the University of Saskatchewan. It serves as an ideal test bed for innovative studies relevant to fusion science and technology. Currently, it is the only device in Canada devoted to magnetic fusion research. Several researches done on STOR-M have been employed in the programs of larger tokamaks. These include Alternating Current tokamak operation [12], Ohmic heating [13], turbulent heating [14], plasma biasing [15] and compact torus injection [16] which has been proposed as a fuelling technique. The main parameters of the STOR-M tokamak are listed in Table 1.1.

STOR-M is equipped with several diagnostics, which is described in more details in the next Chapter. The most relevant to this research is the Ion Doppler Spectrometer (IDS) and the Resonant Magnetic Perturbation (RMP) set up.

Table 1.1: STOR-M tokamak parameters [16].

Parameter	**Symbol**	**Value / Range**
Plasma current	I_p	$20 - 40$ kA
Discharge duration	t_d	50 ms
Toroidal magnetic field	B_ϕ	1 T
Energy Confinement time	τ_E	$1 - 3$ ms
Major radius	R	46 cm
Minor radius	a	12 cm
Electron temperature	T_e	220 eV
Ion temperature	T_i	$50 - 100$ eV

1.3 Goals of this thesis

Tokamak plasma is subject to a number of instabilities. Safety factor q plays a key role in determining plasma equilibrium and stability in tokamaks. In an axisymmetric equilibrium, each magnetic field surface corresponds to a value of safety factor q [17]. Safety factor depicts the helical magnetic field line configuration (i.e. the number of times a magnetic field

line goes around toroidally for each time poloidally). If $q = \frac{m}{n}$, where m and n are intergers, the field line joins up on itself after m toroidal and n poloidal rotations round the torus. Hence m is the poloidal mode number and n, the toroidal mode number.

For a tokamak with a circular cross-section and large aspect ratio [18],

$$q(r) = \frac{rB_\phi}{RB_\theta} \tag{1.4}$$

where r is the minor radius, B_θ is the poloidal magnetic field, R is the major radius and B_ϕ is the toroidal magnetic field. Using Ampere`s law to write the poloidal magnetic field in terms of plasma current I_p, the safety factor for an axially symmetric system at the plasma edge becomes

$$q(a) = \frac{2\pi a^2 B_\phi}{\mu_0 R I_p} \tag{1.5}$$

Stability of plasma requires the safety factor at the center to be greater than 1, $q(0) > 1$ [19]. The radial profile of q usually has its minimum value at or close to the magnetic axis and increases outwards. The q-profile for different plasma current at constant toroidal magnetic field is shown in figure 1.3.

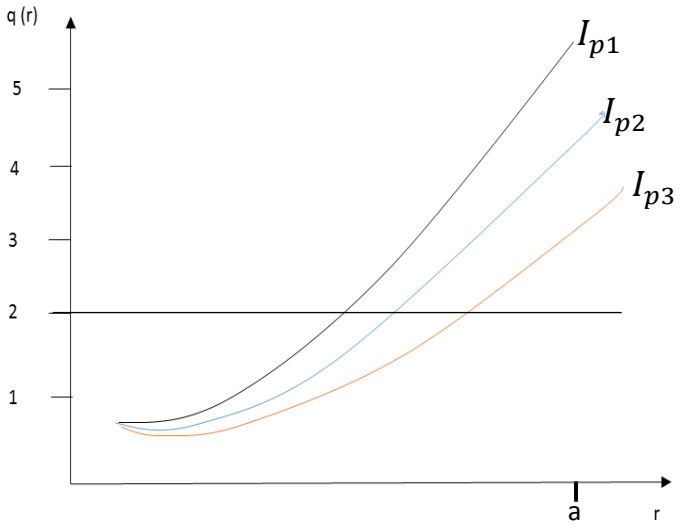

Figure 1.3: Plot showing schematic q-profile with different plasma current. As current increases, safety profile reduces and $q = 2$ surface moves radially outwards. $I_{p3} > I_{p2} > I_{p1}$.

For this research, the effects of changing edge safety factor on the toroidal plasma flow were studied. This was done by increasing the plasma current while keeping the toroidal magnetic field constant. In doing so, the $q = 2$ surface moved radially outward and the effect of RMP and CTI on toroidal plasma flow with varying edge safety factor was investigated. Diagnostics from the IDS was used for the flow measurement.

Plasma flow and fluctuation suppression is very important in tokomak plasma. The $m/n = 2/1$ tearing mode, which takes the form of magnetic islands, grows near the $q = 2$ surface [20]. Also, error fields arise from misalignment of the coils or the internal winding structure, introducing perturbing components to the magnetic field. Spinning the plasma toroidally would substantially diminish the island size and reduces coupling between the

magnetic island and the error field if the angular frequency of rotation is sufficiently higher than the nonlinear growth time of the tearing mode island [21]. It has been observed that, RMP fields induce either electromagnetic torque or neoclassical toroidal viscosity torque resulting in plasma rotation [22]. For very small error fields, this rotation prevents large island growth. This results in stabilizing instabilities in the tokamak plasma.

Previous studies were done with varying RMP current, however for this research, RMP current would be kept constant and plasma current would be varied. The results would be compared with previous measurements for consistency.

1.4 Thesis Outline

This thesis is laid out as follows.

Chapter Two covers the generic description of a tokamak with emphases on STOR-M and its major diagnostics. The structural components of STOR-M as well as their mode of operation will be discussed.

Chapter Three describes the theory behind this study. The features of spectral line shape creation and their analysis is discussed. Also, the broadening mechanisms which the spectral lines are subject to, are described.

Chapter Four describes the design and components of the IDS system installed on

STOR-M. The operating principle of the IDS is outlined. The method of alignment and calibration of the IDS system is explained.

Chapter Five highlights the experimental results of this study. The flow velocity of impurity ions is measured during the application of RMP and CTI. The result is categorized into core emissions and periphery emission.

Chapter Six summarizes the key results of this study.

Chapter Two

STOR-M Tokamak and Diagnostics

2.1 Introduction

In the first chapter, an overview of a generic tokamak was discussed. A more detailed description of the STOR-M tokamak and its major diagnostics will be presented in this chapter. To begin, a brief history of STOR-M will be given, highlighting its key features. This is followed by an overview of each diagnostic and its core operating principle.

2.2 STOR-M Tokamak and Diagnostics

STOR-M tokamak was built following STOR-1 and STOR-1M [23]. Its toroidal coil system was also updated in 1994 to increase the toroidal field strength. The first research experiments can be dated back to 1997 [24] and has logged over 267000 discharges to date. Its vacuum chamber consists of two halves, which are insulated electrically by two ceramic breaks. A stainless steel limiter is used to separate the hot plasma from the inner chamber wall during discharges. The limiter consists of a circular part of radius 13 cm (inboard and outboard) and a pair of horizontal rails at 12 cm (top and bottom). This configuration allows the plasma column ± 1 cm horizontal shift without being scraped off [25]. The chamber is equipped with twenty-three ports for various diagnostics, gas feeding and pumping. There are eleven vertical ports, ten horizontal ports and two tangential ports. One of the horizontal and vertical ports each was used for taking optical measurements in this research. The vacuum pumping system in STOR-M

consists of a rotary pump and a turbo-molecular pump (TMP) connected via a set of valves. The chamber is evacuated to a base pressure of 1×10^{-7} Torr prior to operation. For normal operations, the vacuum chamber is filled with ultra-pure hydrogen (99.999%) to a pressure of about 1.4×10^{-4} Torr. Figure 2.1 shows the side view of the STOR-M tokamak configuration.

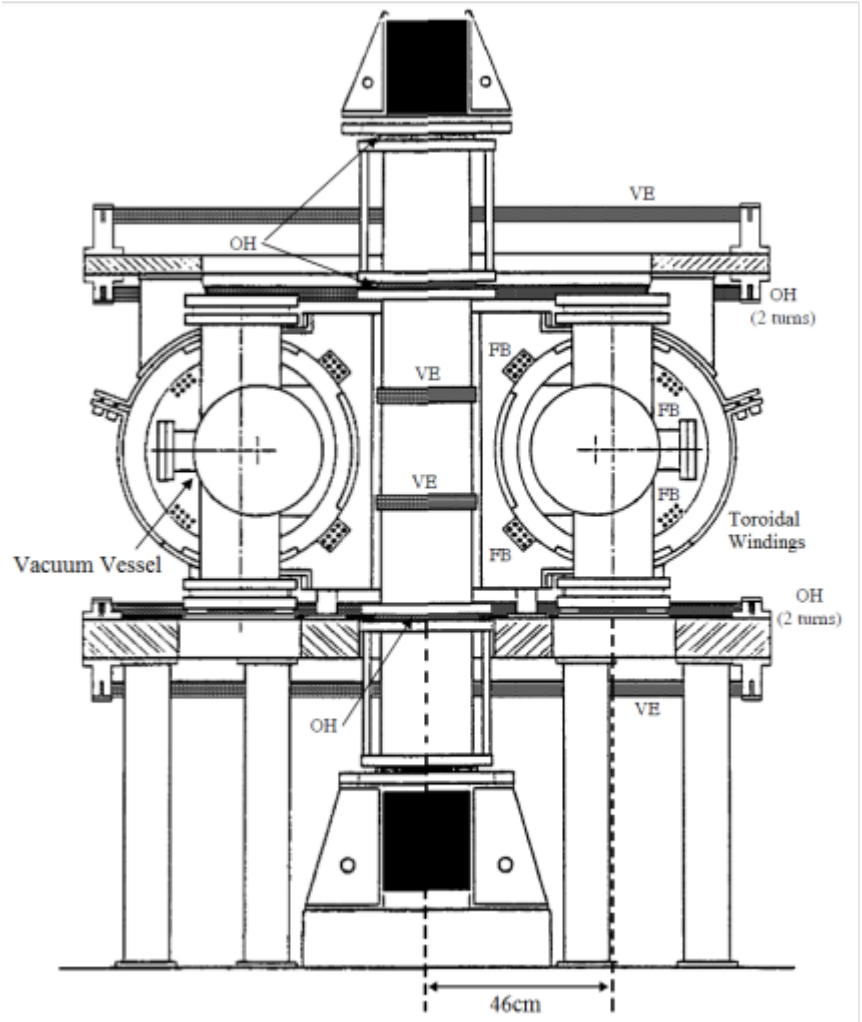

Figure 2.1: Side view of the STOR-M tokamak configuration [25]. OH is the Ohmic primary coils (8 turns), VE represents Vertical Equilibrium field coils and FB are coils for feedback plasma position control and induction coils for fast turbulent heating current.

Charging and discharging capacitor banks in a precise time sequence provide the currents necessary to induce toroidal magnetic field and plasma current. Presently, the capacitor banks are charged in three minutes and discharged in 50 ms during each four-minute operation cycle, to generate and maintain plasma. During each cycle, an Ohmic bias bank is discharged to the main transformer to magnetically saturate the core, maximizing the magnetic flux available for discharge. The B_t bank triggers next through an ignitron delivering up to 12 kA to the toroidal field coil [26]. A hot filament system is used to assist an RF (radiofrequency) system in generating a low temperature RF plasma. Lastly, the fast Ohmic bank is discharged for current buildup followed by a slow bank for maintaining a flat plasma current plateau. The sketches of B_t and Ohmic coil current waveforms are shown in Figure 2.2.

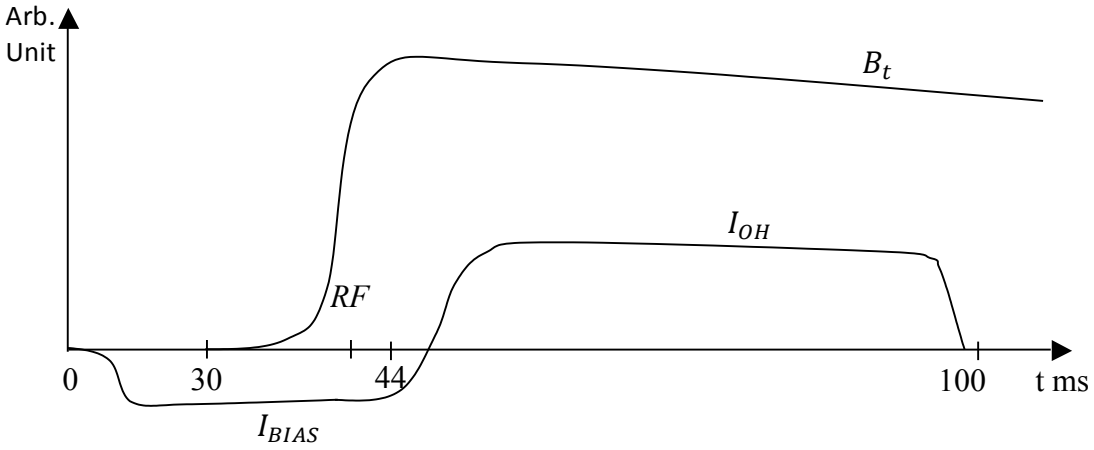

Figure 2.2: Timing parameters for STOR-M discharge [27]. The waveforms of B_t, I_{OH} and I_{BIAS} are shown.

2.3 STOR-M Diagnostics

The discharge parameters in STOR-M are monitored using a standard set of diagnostic equipment. For the majority of the diagnostics, non-invasive techniques are employed. This allows many plasma parameters to be determined without disturbing the plasma significantly. Diagnostic instruments used on STOR-M include: Rogowski coils, voltage pick-up loop, a 4-mm microwave interferometer, position sensing coils, x-ray detectors, Mirnov coils and Langmuir probes. The diagnostics which are routinely used will be described in the next sub-sections. Recent additions to STOR-M diagnostics include an ion Doppler spectroscopy (IDS) system [28] and a resonant magnetic perturbation (RMP) system [29]. The IDS is employed for toroidal plasma flow measurements and the RMP has been used to study the suppression of magnetic islands in STOR-M [30].

2.3.1 Rogowski Coil

The current in the various field windings of the STOR-M tokamak and within the plasma itself is measured with Rogowski coils. A Rogowski coil consists of N turns of wire wound around a closed non-magnetic insulator frame with a uniform cross section. A typical Rogowski coil is illustrated in figure 2.3 where A is the area of a small loop in the windings. When a current I passes through the coil, the generated voltage signal V_{RC}, is proportional to the time rate of change of the magnetic flux Φ

$$V_{RC} = -\frac{d\Phi}{dt} \tag{2.1}$$

Form Faraday`s law of induction, the flux linking the entire coil is given by

$$\Phi = \mu NAI \tag{2.2}$$

where μ is the magnetic permeability. The current enclosed by a Rogowski coil is determined by integrating the picked up voltage as

$$I = -\frac{1}{\mu NA}\int V_{RC}\, dt \tag{2.3}$$

As a measure against pick up of unwanted magnetic flux, a return winding is wound in the opposite toroidal direction on the Rogowski coil. The signals picked up are carried by coaxial cables to the data acquisition system where they are integrated by actively gated integrators. The frequency response of each coil is linear up to 800 kHz [31], which is adequate for measuring current in STOR-M. Homemade coils are calibrated against a commercial Rogowski coil manufactured by Pearson Electronics before installing on STOR-M.

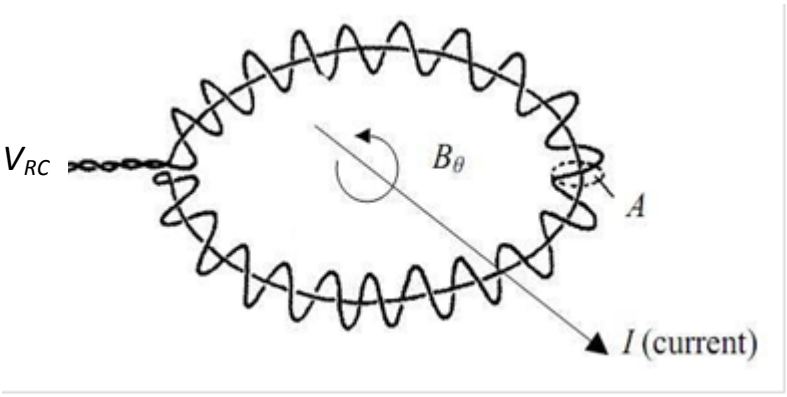

Figure 2.3: Schematic of a typical Rogowski coil [40].

2.3.2 Plasma Loop Voltage

The plasma loop voltage V_p is determined by measuring the voltage of a toroidal loop wire parallel to the plasma current. On STOR-M, a single loop on the top of the vacuum chamber measures the plasma loop voltage. The measured loop voltage arises from both the resistance R_p and the inductance L_p of plasma

$$V_p = I_p R_p + \frac{d(I_p L_p)}{dt} \tag{2.4}$$

In a tokamak, the plasma resistance and plasma inductance are given by [32]

$$R_p = \eta \frac{2\pi R}{\pi a^2} \quad \text{and} \quad L_p = \mu_0 R \left[\ln\left(\frac{8R}{a}\right) + \frac{l_i}{2} - 2\right] \tag{2.5}$$

where R is the major radius of the plasma column, a is the minor radius, η is the plasma resistivity and l_i is the plasma internal inductance parameter expressed as [32]

$$l_i = \frac{\overline{B_\theta^2}}{B_\theta^2(a)} \tag{2.6}$$

The measured voltage is attenuated using a 1: 100 voltage divider and the signal is carried to the control room via triaxial cable where it is connected to a data acquisition system. Figure 2.4 shows a schematic diagram of the loop voltage circuit on STOR-M.

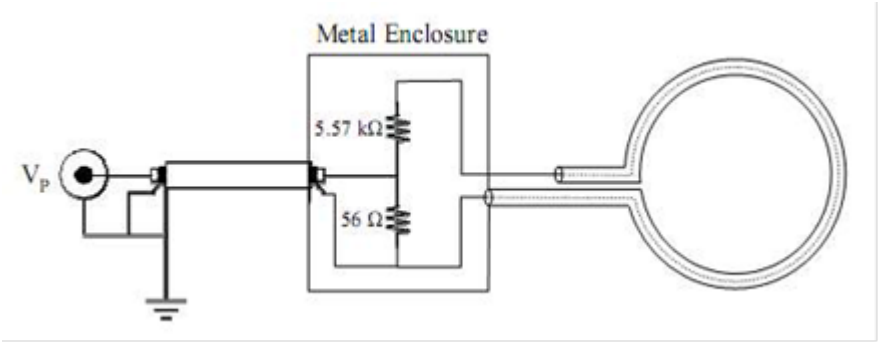

Figure 2.4: Schematic of a voltage pick-up loop circuit on STOR-M [33].

2.3.3 Position Sensing Coils

The quality of a plasma discharge depends on the position of plasma column within the vacuum vessel. The position of the plasma column is measured in STOR-M using six magnetic probes located immediately outside the vacuum vessel. Four probes separated poloidally by 90° and oriented at the minor radius of 17 cm detect the poloidal magnetic field. The other two, oriented above and below the vacuum vessel, detect radial magnetic field. The orientation of these six probes is illustrated in Figure 2.5.

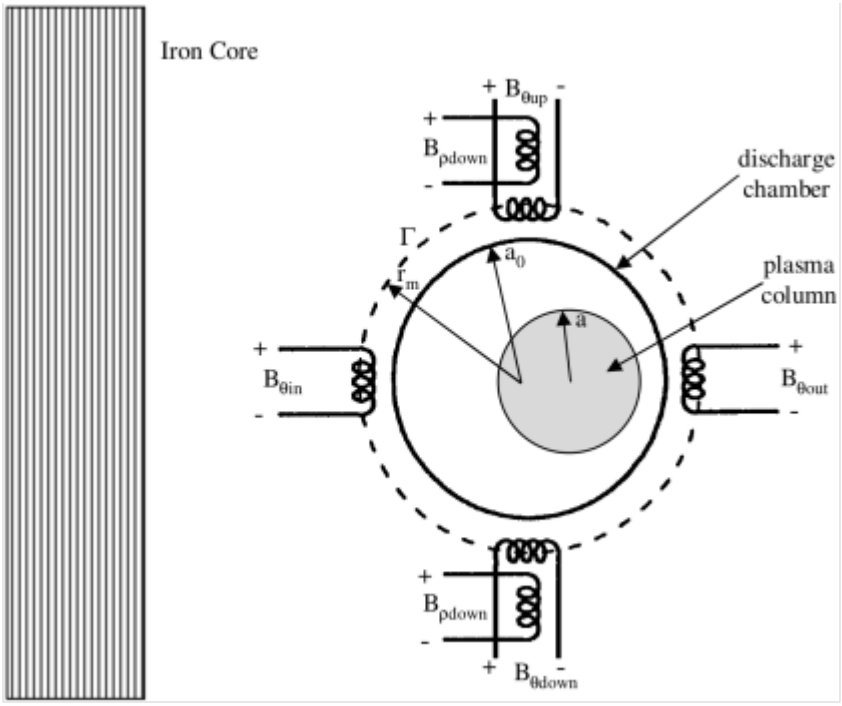

Figure 2.5: Plasma position sensing coils on STOR-M [29]. The six probes together detect poloidal and radial magnetic field. The magnetic probe signals must be compensated for unwanted magnetic field using compensation circuits.

In addition to detecting magnetic field produced by the plasma current, the position sensing coils pick up unwanted fields. This is primarily due to misalignment and imperfections of the toroidal coil system. These stray magnetic fields are eliminated using compensation

circuits, from which their current waveform are added to sensing coil signals with appropriate amplitudes and polarities [34].

2.3.4 Mirnov Coils

A Mirnov coil is a modified Rogowski coil with a variable winding density around the loop [32]. This special arrangement of the coils permits measurement of specific modes of B_θ oscillations. In tokamaks, B_θ can be Fourier expanded as

$$B_\theta(\theta) = B_0 + \sum_{m=1}^{\infty} (C_m \cos(m\theta) + S_m \sin(m\theta)) \tag{2.7}$$

where B_0 is the unperturbed field. The periodicity in the magnetic fluctuations is because the solution must be periodic around the poloidal angle θ.

In total, a set of thirty-two discrete Mirnov coils have been installed on STOR-M. The coils are arranged into four poloidal arrays tailored to measure different modes of fluctuations. The relation between the spatial resolution of arrays and the poloidal mode numbers is expressed as the total number of coils divided by 2 $(\text{i.e., total number of coils}/2)$. Two of the arrays have twelve Mirnov coils poloidally separated by 30°. These two arrays can detect poloidal mode numbers up to $m = 6$. The remaining two arrays contain four coils each, poloidally separated by 90°. This permits measuring poloidal mode numbers up to $m = 2$. One coil from each of the poloidal array is configured to form a 4-coil toroidal array. This enables detection of toroidal mode numbers $n = 1$ and $n = 2$, which are dominant toroidal modes in STOR-M [35]. Figure 2.6 shows a schematic of the locations of the Mirnov arrays on STOR-M.

The magnetic signals from the Mirnov coils are transmitted to an aluminum breakout box where they are terminated by 50 Ω resistors. The signals are then conveyed to the data acquisition system via coaxial cables. The data acquisition system is equipped with 14 bit digitizers from National Instruments. The digitizers have a sampling rate of up to 1 MHz [36] and are controlled by a LabVIEW program. The raw Mirnov signals are analyzed using a MATLAB numerical analyses code which has already been developed.

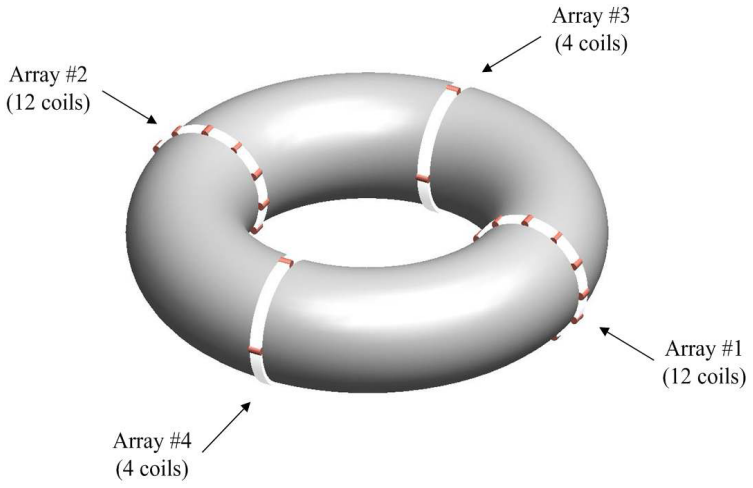

Figure 2.6: (a) Mirnov array configuration in STOR-M [29]. Four arrays are used. Arrays #1 and #2 each has 12 coils, while Arrays #3 and #4 have 4 coils each.

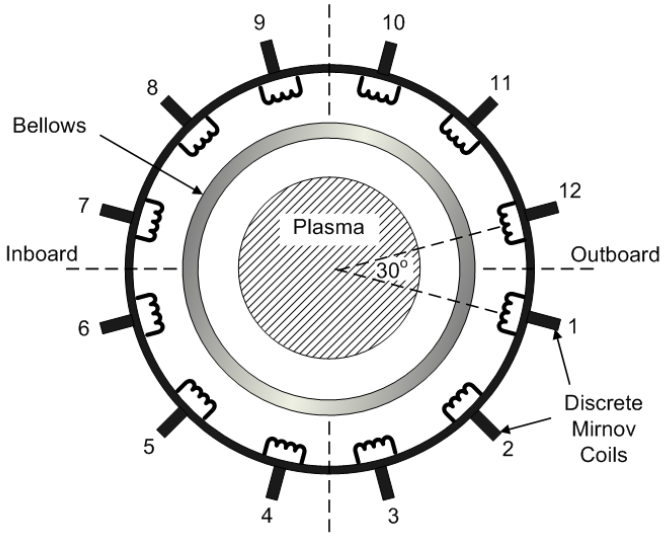

(b) Coils configuration of arrays #1 and #2 [35]. Coils are poloidally separated by 30°

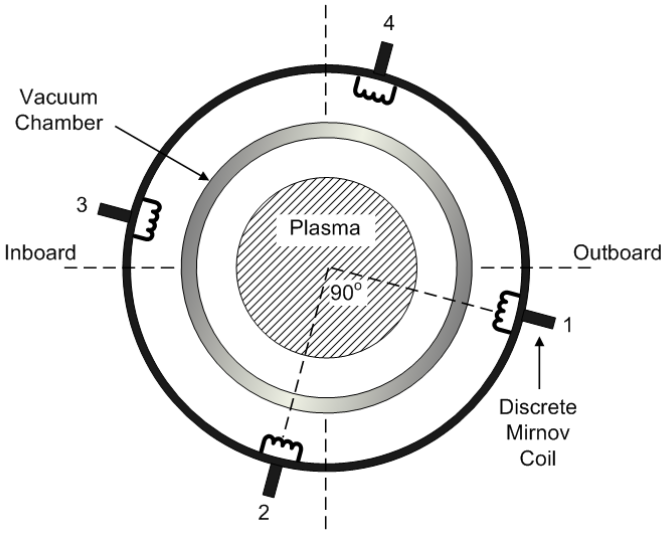

(c) Coils configuration of arrays #3 and #4 [35]. Coils are poloidally separated by 90°.

2.3.5 Ion Doppler Spectroscopy (IDS) System

The IDS system is a novel technique which permits non-invasive measurements of plasma flow velocity using different ion impurities. The IDS system on STOR-M is constructed on a SPEX 1702 0.75-meter spectrometer. It is a symmetrical Czerny-Turner spectrometer with a diffraction grating of 1200 grooves/mm and blazed at 5000 Å [37]. It consists of two concave mirrors with equal focal lengths. Light is transmitted from the plasma to the spectrometer using an optical fiber. At the spectrometer end, the light is dispersed and further magnified by a fused silica cylindrical rod lens at the exit of the spectrometer. The magnified spectrum is detected by a 16-channel photomultiplier tube (PMT) array enclosed in a light tight aluminium box. The current signal from the PMT is converted to voltage signal using a current-voltage preamplifier built on operational amplifiers. The voltage signals are conveyed to the data acquisition system via coaxial cables. The plasma flow velocity is estimated from the spectroscopic measurement of the Doppler line wavelength shift. The unshifted wavelength is measured from a normal port on STOR-M tokamak, and the Doppler shifted wavelength is obtained from a tangential port. The mechanism of plasma flow will be discussed in the next chapter. Figure 2.7 shows the setup of the IDS system installed on STOR-M. For spectroscopic measurements in STOR-M, three lines; C_{III}, O_V and C_{VI} are used. These lines are relatively stronger than other emission lines and possess a reasonable signal level in STOR-M [28]. In STOR-M, C_{III} is located at the plasma edge, while O_V and C_{VI} are near the plasma core due to the intrinsic radial profile of the electron temperature in the plasma.

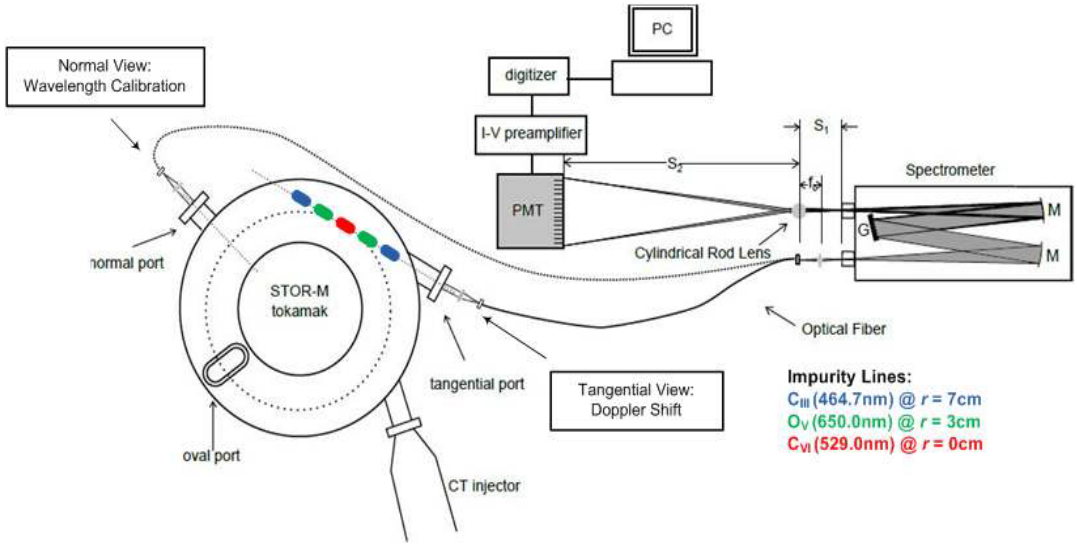

Figure 2.7: Setup of the IDS system installed on STOR-M [29]. Targeted impurity lines and the corresponding radial position are also shown. Blue is for C_{III}, green O_V and red C_{VI}. Note that the locations of the peak emission radial location are only for plasma current 22 kA.

2.3.6 Resonant Magnetic Perturbation (RMP) System

An RMP system has been installed on STOR-M, currently for magnetic fluctuation suppression studies. The system consists of two helical windings around the vacuum chamber poloidally separated by 90° [29, 30]. The RMP field is produced by driving a current pulse with equal magnitudes but opposite direction through the two sets of windings. This cancels out induction effect and transformer effect to and from other coils in the tokamak circuits and plasma current in particular [30]. The current pulse is generated with capacitor banks and gated by an IGBT or SCR switch. For the present setup, the RMP circuit produces slow RMP (SRMP) and fast RMP (FRMP) pulses. The SRMP pulse has a nearly constant current of 1 kA and duration of 8 ms whereas the

FRMP pulse is 1.5 kA and lasts for about 0.5 ms. The FRMP is typically fired during the SRMP current flat-top.

To achieve resonant interaction, the coils have to be configured in such a way that their helicities match the helicity of the magnetic perturbations (islands). The RMP coil installed on STOR-M targets the $(2, 1)$ magnetic perturbation [29, 30]. The current generated by the RMP pulses are measured with a Rogowski coil positioned at the low branch of a $1{:}\,9$ current divider. Figure 2.8 shows the layout of the RMP coils installed on STOR-M. The current waveform is then sent to the data acquisition system using a coaxial cable where it is attenuated by a standard 10× BNC attenuator.

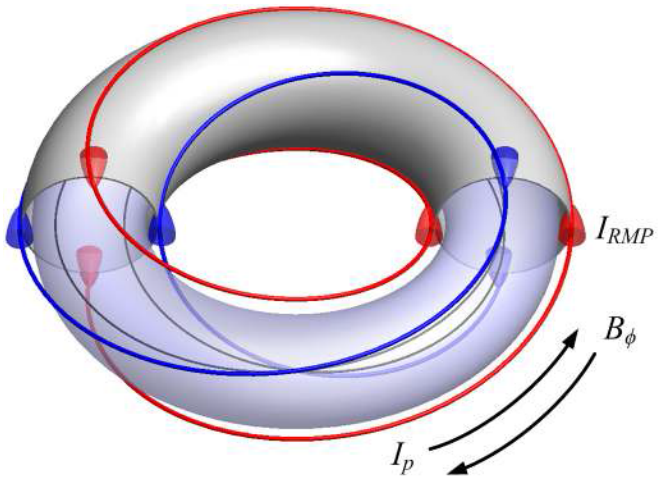

Figure 2.8: Configuration of RMP coils on STOR-M [35]. Two set of windings (red and blue) with opposite polarities are used to cancel induction current and minimize coupling between the resonant coils and other coils.

Chapter Three

Plasma Flow and Line Emission Spectra Analysis

3.1 Introduction

This chapter focuses mainly on the theories and physics underlying this research. The concept of impurity emission will be developed and this concept will be used as a basis for establishing the mechanism of plasma flow. Later in this chapter, insight on Doppler shift and spectral line broadening will be given.

3.2 Flow Measurements in STOR-M

Plasma flow velocity can be measured by various means. Typical diagnostics are Mach probes and Doppler spectroscopy. Earlier flow measurements in STOR-M were carried out using Mach probes which is essentially a bi-directional Langmuir probe set. The Mach probes measure plasma flow parallel and perpendicular to the magnetic field [38]. These measurements are relevant to study flows induced by biasing experiments. In the presence of a mean plasma flow, the Mach probe is biased in the ion saturation currents at specific angular directions [39]. The ratio of the upstream ion saturation currents j_u to the downstream ion saturation currents j_d is given as [40]

$$\frac{j_u}{j_d} = exp(KM) \tag{3.1}$$

where K is a calibration constant dependent on T_e and T_i, and M is the Mach number. The plasma flow velocity can then be deduced from the asymmetry of the saturation currents between the upstream and downstream probes. Equation (3.1) holds if the ion temperature is on the same order or larger than the electron temperature $T_i/ZT_e \gg 1$ where Z is the ionization state [41]. The Mach number gives a good estimate of the flow speed in units of ion sound speed [42]

$$M = \frac{v_d}{c_s} = \frac{1}{K}\ln\left(\frac{j_u}{j_d}\right) \tag{3.2}$$

The Mach probes can merely measure flow velocity at the plasma edge or in the scrap-off-layer (SOL) region and also, it needs to be inserted inside the plasma for measurement.

The Ion Doppler Spectroscopy (IDS) is a non-intrusive diagnostic method and the system installed on STOR-M is mechanically isolated from the tokamak. In contrast to the relatively simpler design and operation of Mach probes, the IDS system is made up of delicate optical components and can be electrically and mechanically separated from the tokamak. Its working principle is based on the Doppler effect, a technique which enables the measurement of velocities of moving light emitting sources. The wavelength of light emitted by a moving object changes due to the relative motion between the object and the observer. The Doppler wavelength shift of spectral lines occur when the source emitting the line radiation is moving away (red-shift) from or moving towards (blue-shift) the observer. Since this study was carried out using the IDS, the remainder of this this thesis will focus mainly on this system.

3.3 Physics of IDS

As mentioned earlier, the principle behind the operation of the IDS is the Doppler effect. The IDS system observes well-defined spectral lines from impurity ions in magnetic confined plasma. Fusion plasmas are typically generated from ionization of a neutral gas. In most cases isotopes of hydrogen are used as the plasma fuel. However, in any fusion device, other types of ions (impurities) are also present. Impurity ions in fusion devices can originate from various sources such as organic materials used for fabricating probes inserted into the chamber, sputtering from chamber walls, as well as outgassing from the chamber walls. They also exist naturally due to the inability to achieve a perfect vacuum in a fusion reactor before fuelling [43]. In effect, elements such as nitrogen, oxygen and carbon can be found in small quantities in typical plasma discharges. Atoms and ions of the hydrogen and trace impurities emit radiation when transitions of electron occur between the various energy levels of the atomic system. Unlike the continuum of free-electron radiation such as Bremsstrahlung, this radiation is in the form of narrow spectral lines subject to a number of broadening mechanisms. Valuable and often quite accurate diagnostic information can be obtained from these bound-electron radiations. In the STOR-M tokamak, properties of the impurity ions are closely related to that of the hydrogen ions due to the strong interaction among the ion species. Thus, impurity ion velocity measurement can in principle provide direct information about the hydrogen ions, which is the main working gas.

Carbon and oxygen ions have been observed in STOR-M during discharges. These ions have multiple ionization states with higher ionization states more abundant at higher electron temperature. The average electron temperature (with peaked temperature distribution at the

center) has been estimated to be 220 eV in the STOR-M tokamak [25]. At this temperature, oxygen and carbon emission lines should be observable from lower ionization states to C_{VI} and O_{VIII}. Figures 3.1 and 3.2 show the abundance of oxygen and carbon ionization states at different electron temperatures.

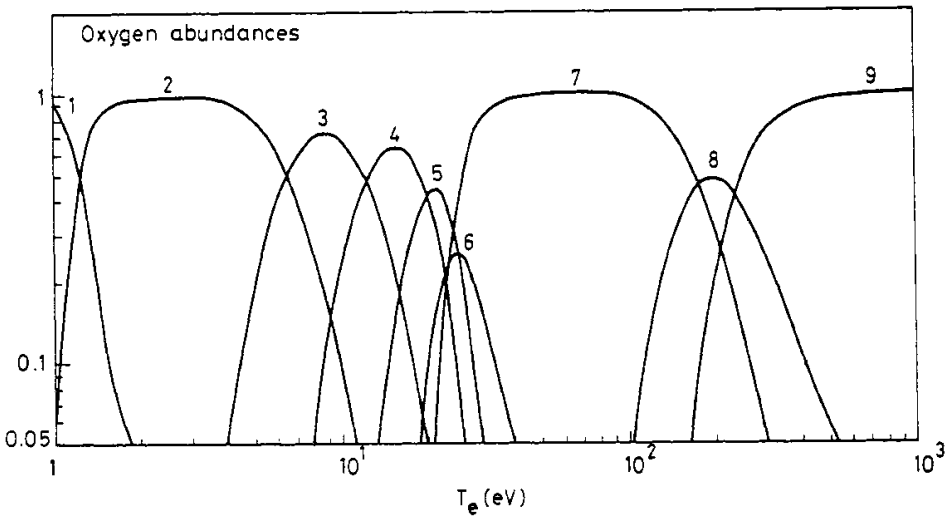

Figure 3.1: Abundance of oxygen at different electron temperature [44]. Between electron temperature range $1 - 1000$ eV, oxygen is observable from O_I to O_{IX}.

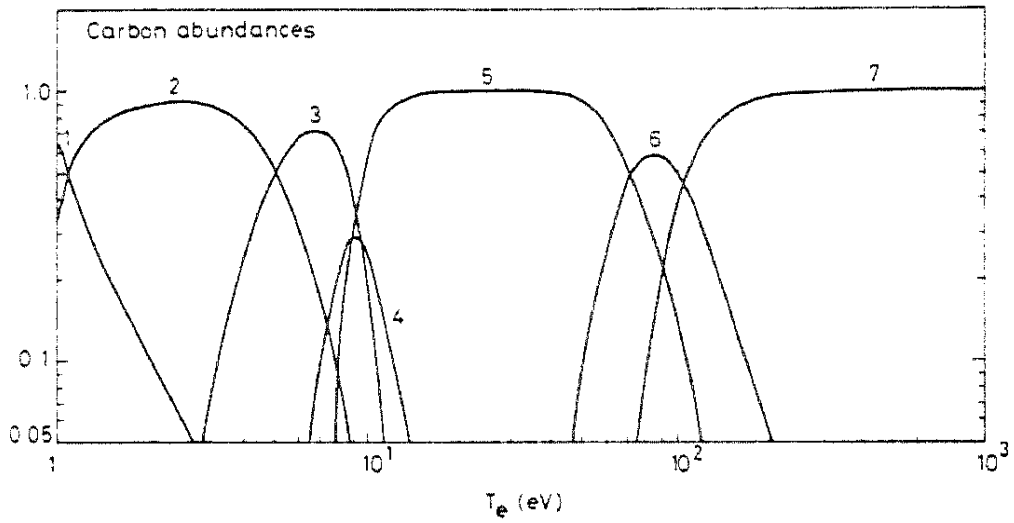

Figure 3.2: Abundance of carbon with electron temperature [44]. Between electron temperature range $1 - 1000$ eV, carbon can be observed from C_I to C_{VII}.

Previous study on STOR-M indicates the presence of C_{III}, O_V and C_{VI} at significant levels. The local emissivity profile of the ions is shown in Figure 3.3. The tokamak has higher electron temperature at the centre than the edge corresponding to different spatial locations of the observed ions within the STOR-M plasma. As expected, C_{III} is located at the periphery, while O_V and C_{VI} are located at the core. The emission profile measurements were for a plasma current of about 22 kA. The peak emission locations are expected to move towards the center when the plasma current decreases and the electron temperature decreases accordingly. For very low plasma current, the high ionization states may not be present due to low temperatures expected.

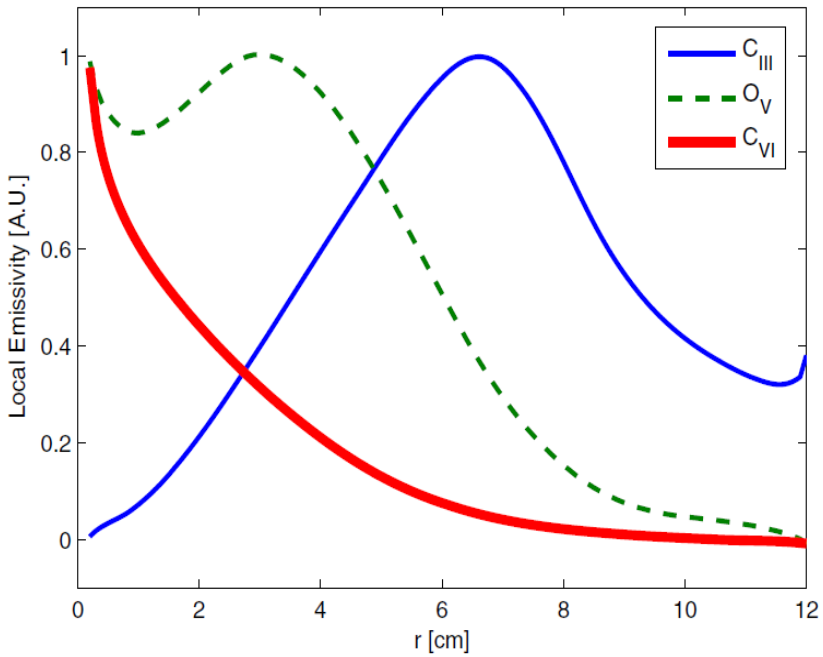

Figure 3.3: The radial profile of three emission lines in STOR-M for plasma current of about 22 kA [28]. From this profile, it can be seen that, the C_{III} emission line is peaked around $r = 7$ cm, O_V at $r = 3$ cm while C_{VI} is peaked at the chamber center.

3.4 Mechanism of Plasma Flow

Plasma rotation is important in many aspects of tokamak development and has been an active field of research on many magnetic confinement devices. Due to the much larger ion mass m_i than the electron mass m_e, flow velocity in plasma is essentially equal to the ion velocity

$$\boldsymbol{v} = \frac{m_i \boldsymbol{v_i} + m_e \boldsymbol{v_e}}{m_i + m_e} \approx \boldsymbol{v_i} \tag{3.3}$$

where $\boldsymbol{v}, \boldsymbol{v_i}$ and $\boldsymbol{v_e}$ are the plasma, majority ion and electron velocities. In tokamaks, plasma flow velocity can be decomposed into geometric directions (poloidal or toroidal) or into parallel and perpendicular directions with respect to the total magnetic field. These two decompositions are illustrated in Figure 3.4. For this study, the geometric decomposition will be employed with much emphasis on the toroidal flow.

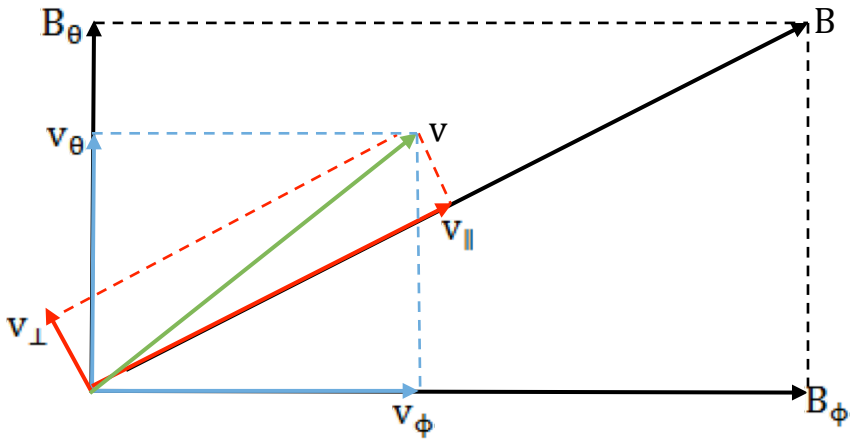

Figure 3.4: Velocity decomposition for plasma flow [29]. The velocity components of plasma flow can be decomposed with respect to tokamak coordinates or with respect to the total magnetic field.

In order to examine the mechanism of plasma flow in tokamaks, the behaviour of particles in electric field $\boldsymbol{E}$ and magnetic field $\boldsymbol{B}$ needs to be analyzed. In the presence of magnetic field only, a charged particle exhibits a circular gyration about a fixed guiding center with frequency

$$\omega_c = \frac{qB}{m} \tag{3.4}$$

where q is the charge of the particle, B is the magnitude magnetic field and m the mass of the particle. The direction of the gyration is always such that the magnetic field generated by the charged particle is opposite to the externally imposed field. This behaviour explains the diamagnetic nature of plasmas.

However, in the presence of both electric and magnetic fields as in tokamaks, there is a drift of the guiding center in addition to the circular gyration. The equation of motion is given as

$$mn\frac{d\boldsymbol{v}}{dt} = qn(\boldsymbol{E} + \boldsymbol{v}\times\boldsymbol{B}) \tag{3.5}$$

To obtain the drift of the guiding center, the $m\frac{d\boldsymbol{v}}{dt}$ term can be omitted since it gives only the circular motion at frequency ω_c [45]. In a plasma fluid, the equation of motion is

$$mn\left(\frac{\partial \boldsymbol{v}}{\partial t} + \boldsymbol{v}.\nabla\boldsymbol{v}\right) = qn(\boldsymbol{E} + \boldsymbol{v}\times\boldsymbol{B}) - \nabla p \tag{3.6}$$

From this equation, equation (3.5) then becomes

$$qn(\boldsymbol{E} + \boldsymbol{v}\times\boldsymbol{B}) - \nabla p = 0 \tag{3.7}$$

Taking cross product with $\boldsymbol{B}$ and solving for the transverse component gives

$$\boldsymbol{v}_{\perp} = \frac{\boldsymbol{E}\times\boldsymbol{B}}{B^2} + \frac{1}{qn}\frac{\boldsymbol{B}\times\nabla p}{B^2} \tag{3.8}$$

The first term is the drift of the guiding center $\boldsymbol{v_E}$ and is independent of the charge or mass of the particle. The second term is the diamagnetic drift velocity. The effect of the toroidal electric field E_ϕ on the flow is fairly small as it mostly drives electron rather than ions [46]. The radial electric field E_r, hence is the main contribution to the plasma flow. The shape of the tokamak chamber also causes an inhomogeneity in the toroidal magnetic field, which varies radially as

$$B_\phi \approx B_o\left(1 - \frac{r}{R}\cos\theta\right) \tag{3.9}$$

where $\frac{r}{R}$ is the inverse aspect ratio and θ is the poloidal angle. The toroidal magnetic field is stronger in the inner side of the tokamak as compared to the outer side. This causes a peroidic variation in the poloidal plasma flow known as magnetic pumping [47]. The poloidal rotation is thus damped, except for the neoclassical contribution due to the ion temperature gradient [48]. Taking all these into account, the toroidal plasma velocity can be obtained from the radial component of Equation (3.8) as

$$v_\phi = \frac{1}{B_\theta}\left(E_r - \frac{1}{q}\frac{dp}{dr}\right) \tag{3.10}$$

where positive flow is defined along the plasma current direction and both E_r and $\frac{dp}{dr}$ are negative. The two effects on the flow velocity direction are opposite. The inverse relation between the toroidal flow and the poloidal magnetic field can be used to determine the direction

of flow. Since the plasma current generates the poloidal magnetic field, reversing the direction of plasma current causes a reversal of the poloidal magnetic field and subsequently, the direction of the toroidal flow. This effect has been observed in STOR-M as well as other tokamaks. In the edge region, v_ϕ is in the same direction as plasma current, however, the flow is reversed in the core region.

3.5 Spectral Line Shape Analysis

Characteristics of the spectral line shape act as a diagnostic for various physical parameters of the plasma in which the emitting species is embedded. Also, in order to fit experimental data to a particular model, the various mechanisms which determine the line shape and position need to be explored. The spectral lines are subject to several possible broadening mechanisms. These include Doppler shift and broadening, Instrumental broadening, Natural broadening, Stark broadening and Zeeman splitting. A brief description of each broadening mechanism will be given.

3.5.1 Instrumental Broadening

This is mainly due to setup of the spectrometer used for measurements. Properties of the spectrometer affect the quality of spectrum recorded. To investigate instrumental broadening, the spectral line of a known light source is needed. For this study, a mercury wavelength calibration lamp is used. Hypothetically, the line profile for instrumental broadening is triangular or

trapezoid [49]. However, for small entrance slit widths, the line profile for instrumental broadening can be described by a Gaussian function. A typical model to characterize the instrumental function of the spectrometer used in this study is

$$L(\lambda) = Aexp\left(-\frac{(\lambda - \lambda_o)^2}{2\sigma^2}\right) \tag{3.11}$$

where A is the amplitude and λ_o is the central wavelength of the emission line. The full width at half maximum is

$$\Delta\lambda_{FWHM} = 2.354\sigma \tag{3.12}$$

where σ is the standard deviation. The standard deviation varies with the entrance and exit (or PMT detector) widths of the spectrometer. Figure 3.5 shows the relationship between measured instrumental broadening and the input slit width for the mercury calibration lamp. For optimal results, the instrumental profile width should be made as small as possible while preserving a significant signal level.

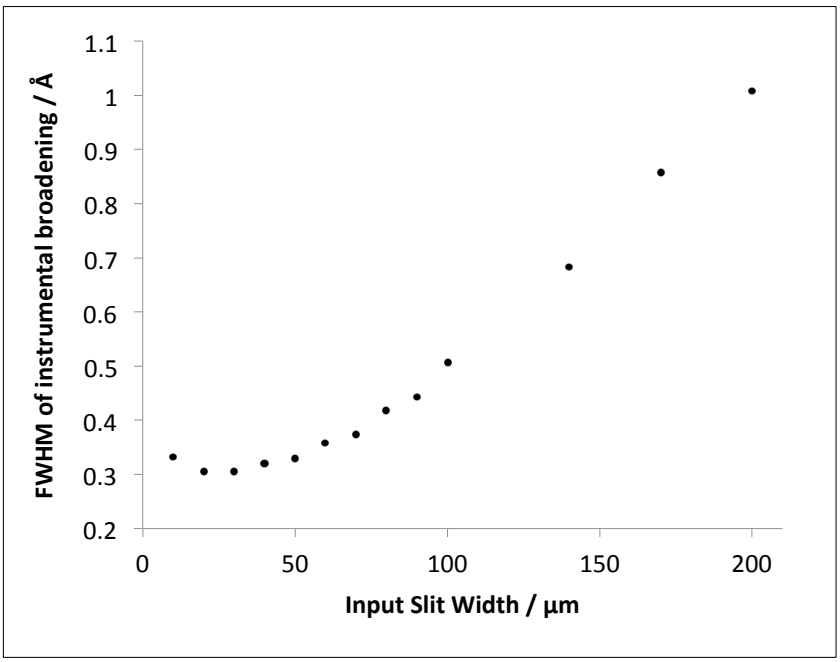

Figure 3.5: Plot showing instrumental broadening with increasing input slit width. In the range of 10 µm to 200µm for input slit width, the instrumental broadening varies from 0.3 Å to 1.0 Å.

3.5.2 Doppler Shift and Broadening

The Doppler shift of spectral line provides a measure of the flow velocity of plasma. The IDS system observes well-defined spectral lines from impurity ions in magnetically confined plasma. The wavelength of light emitted by a moving source is perceived by an observer at rest to be different than it is in the frame of the source. For a source moving relative to an observer, it is necessary to account for the effect of the difference between the proper time measured by the moving source and the coordinate time measured in the observer's frame. This is known as time dilation.

The light frequency ν_o emitted by a source moving at velocity v is seen in an observer's frame as

$$\nu = \frac{\sqrt{1+\beta}}{\sqrt{1-\beta}}\nu_o \tag{3.13}$$

where $= \frac{v}{c}$, c being the speed of light. Since the emitting specie's velocity is much smaller than the speed of light, the invocation of special relativity is not necessary and classical treatment of the Doppler effect should suffice. The first order approximation after applying binomial expansion to equation (3.13) is

$$\nu = \left(1 + \frac{v}{c}\right)\nu_o \tag{3.14}$$

Rearranging the terms in equation (3.14) gives

$$\Delta\nu = \nu - \nu_o = \frac{v}{c}\nu_o \tag{3.15}$$

Experimentally, the wavelength λ of a light source is more feasible and is related to frequency as

$$\lambda\nu = c \tag{3.16}$$

Taking the derivative of equation (3.16) by applying the chain rule gives

$$\frac{\Delta\lambda}{\lambda} = -\frac{\Delta\nu}{\nu} \tag{3.17}$$

For a plasma moving towards or away from the observer, a given spectral line will experience a shift in wavelength given by

$$\Delta\lambda = -\frac{v}{c}\lambda_o \tag{3.18}$$

The net flow velocity can be determined from the line shift. In the derivation, it was assumed implicitly that all the emitting ions in the plasma have the same velocity. This implies that the plasma has zero ion temperature which is unphysical [50]. To consider the effects of temperature, a distribution of ion velocities is needed. As temperature increases, there is an increasing spread in the distribution of particle velocities. As a result, the light emitted by individual particles has slightly different Doppler shifts. This results in Doppler broadening of the spectral lines.

In plasmas with some equilibrium ion temperature, the velocities of particles of mass m is known to follow the Maxwellian distribution $f(v)$. The Maxwellian distribution of particle velocity is in general 3-dimensional

$$f(v) = n\left(\frac{m}{2\pi kT}\right)^{\frac{3}{2}} exp\left(-\frac{mv^2}{2kT}\right) \tag{3.19}$$

where n is the number of particles per unit volume in the system and k is the Boltzmann constant. For IDS measurements, the Doppler shift along a fixed line of sight is observed. Hence the distribution of only one component of velocity is needed. In one dimension, the Maxwellian velocity distribution for the radiating impurity ion becomes

$$f(v) = n\left(\frac{m}{2\pi kT}\right)^{\frac{1}{2}} exp\left(-\frac{mv^2}{2kT}\right) \tag{3.20}$$

The radiating particle in the line of sight emits light with velocity v according to equation (3.14) as $\left[{}^{v}/_{v_o} - 1\right]c$. This gives a line shape $I(v)$ proportional to the velocity distribution function as

$$I(v) \propto f\left(\left[\frac{v}{v_o} - 1\right]c\right) \tag{3.21}$$

Making this substitution, the Maxwellian velocity distribution yields a Gaussian line profile

$$I(v) = I_o exp\left(-\frac{m(v_o - v)^2 c^2}{2kTv_o^2}\right) \tag{3.22}$$

where I_o is the peak intensity. The width of this Gaussian profile depends on temperature T. The full width at half maximum is calculated by equating the exponential term to ${}^{1}/_{2}$. This gives

$$\frac{\Delta v_{FWHM}}{v_o} = 2\left(\frac{2kT \ln 2}{mc^2}\right)^{\frac{1}{2}} \tag{3.23}$$

from which an estimate of the ion temperature can be found. An expression in terms of wavelength is needed for greater practical utility. For small fractional widths,

$${}^{\Delta\lambda}/_{\lambda} = {}^{\Delta v}/_{v} \tag{3.24}$$

Using the above relation gives

$$\frac{\Delta\lambda_{FWHM}}{\lambda_o} = 2\left(\frac{2kT \ln 2}{mc^2}\right)^{\frac{1}{2}} \tag{3.25}$$

The ion temperature can be estimated from equation (3.25) as

$$T = \frac{\Delta\lambda_{FWHM}^2 c^2}{8k\lambda_o^2 \ln 2} m \tag{3.26}$$

In effect, measuring the line width permits the determination of the ion temperature, and measuring the line shift allows an estimate of the net flow.

3.5.3 Natural Broadening

The mechanism of natural broadening is governed by the Heisenberg uncertainty principle. The quantum states of atoms have a small spread in energy which can be explained as follows. The lifetime of an atom in an upper state is finite due to spontaneous transitions to lower states. The effective spread in energy of a quantum state is given by the uncertainty principle as

$$\Delta E \Delta\tau \geq \frac{\hbar}{2} \tag{3.27}$$

This leads to an uncertainty in the exact energy level of an electron in the excited state resulting in an effective broadening of the line shape. Neglecting induced transitions, the lifetime of the excited state will be [51]

$$\tau = \frac{1}{\sum_{j<i} A_{ij}} \tag{3.28}$$

where A_{ij} is the spontaneous transition rates from state i to state j. The line shape is a Fourier transform of the square root of the exponentially decaying probability of the electron in the ith state [52]. The resulting line shape is a Lorentzian

$$I(\nu) = I(\nu)\frac{1}{1 + [(\nu - \nu_o)2\pi\tau]^2} \tag{3.29}$$

where ν is the frequency of the emitted light. Natural broadening is usually negligible in the visible but can become important for the extreme ultraviolet lines of highly ionized impurities [32]. It is several orders of magnitude smaller than Doppler broadening.

3.5.4 Stark Broadening

Stark broadening is a form of the more general pressure broadening. It is due to the effective collisions via an electric field of an emitting particle and a particle within its vicinity. When an external electric field is stronger than the internal field of an atom, there is a resulting perturbation and splitting of the energy levels of the atom. Two main approaches have been developed to address this broadening effect.

The collisional approach developed by Lorentz [53] supposes that the atom radiates undisturbed for most of the time. However, there are occasional collisions between fast electrons and the radiator which causes the emission to be interrupted and undergoes a phase change. This shows up as broadening of the line. This approach also assumes that the duration of the collision is much less than the mean time between the collisions. Due to the statistical nature of the time between collisions, the collisional event can be modelled as a Poison statistic. The coherence of the wave falls off as $exp\left(-{}^{t}/_{\tau}\right)$ which as in the natural broadening case results in a Lorentzian line shape.

At the other extreme is the quasistatic approach developed by Holtzmark [54]. The atom is assumed to radiate in an environment that is static, yet perturbed during the period of emission. The most significant perturbing effect is due to the electric field of neighboring particles. This also causes the atomic levels in the radiating atom to be perturbed. The radiator thus experiences an instantaneous shift in wavelength, and the average over all possible perturbations gives the line width and shape. This approach, contrary to the approach by Lorentz, assumes that the collision duration is much greater than the mean time between collisions. Using the nearest neighbor approximation to Stark broadening [32], the scaling of the broadening is approximated as $(\nu) \propto (\Delta\nu)^{-\frac{5}{2}}$. There is a more intuitive and compact derivation [55] which is more advanced for the scope of this study.

Due to the difference in velocities of electrons and ions, the electron effects are best modelled using the collisional approximation, while ion perturbations are usually approximated by the quasistatic approach. In high temperature plasmas of moderate density typical of magnetic fusion, Stark broadening is negligible compared to Doppler broadening.

3.5.5 Zeeman Effect

Just as there is energy level perturbation and splitting for atoms in an electric field, a similar effect occurs for atoms in a magnetic field. The magnetic field in a tokamak can split the energy levels in atoms or ions into multiple components, making it energetically degenerate. The

difference between energy levels ΔE is proportional to the magnetic field B. The number of levels also depends on the magnetic quantum number m_l

$$\Delta E = m_l \mu_B B \tag{3.30}$$

where μ_B is Bohr magneton, a physical constant (9.27×10^{-24} J/T) and natural unit for expressing an electron magnetic dipole moment.

The displacement of the energy levels results in spectral lines from electron transitions between the energy levels to also split. This leads to an apparent broadening of the spectral line. In the simplest case, the wavelength can be split into three: $\lambda - \Delta\lambda$, λ and $\lambda + \Delta\lambda$

$$\Delta\lambda = \frac{\lambda^2}{c}\frac{\Delta E}{h} \tag{3.31}$$

where c is the speed of light and h is Planck`s constant. The wavelength shift $\Delta\lambda$ due to Zeeman broadening for C_{III} is calculated to be 0.1 Å, based on STOR-M parameters.

3.6 Combining Broadening Mechanisms

The various types of spectral broadening will be used as a guideline for developing a suitable line shape to fit the experimental data. In reality, all or most of the above broadening mechanisms will be present simultaneously. However, some contributions are more dominant than others. Given the parameters of STOR-M, the most significant contributions are from instrumental broadening and Doppler broadening. The superposition of these broadening effects

is a convolution of the line profile functions. The Doppler broadening as discussed can be modelled by a Gaussian $f(x)$ with mean μ_f and standard deviation σ_f

$$f(x) = \frac{1}{\sqrt{2\pi}\sigma_f} e^{-\frac{(x-\mu_f)^2}{2\sigma_f^2}} \tag{3.32}$$

For this study, the spectrometer is operated at small entrance slit width. This implies that the instrumental broadening can also be modelled as another Gaussian $g(x)$ with mean μ_g and standard deviation σ_g

$$g(x) = \frac{1}{\sqrt{2\pi}\sigma_f} e^{-\frac{(x-\mu_g)^2}{2\sigma_g^2}} \tag{3.33}$$

The convolution of the two functions is shown below. The usual approach is to use convolution theorem [56]

$$F^{-1}\left[F\left(f(x)\right)F\left(g(x)\right)\right] = f(x) \otimes g(x) \tag{3.34}$$

where F is the Fourier transform

$$F\left(f(x)\right) = \int_{-\infty}^{\infty} f(x)\, e^{-i2\pi kx} dx \tag{3.35}$$

and F^{-1} is the inverse Fourier transform

$$F^{-1}\left(F(k)\right) = \int_{-\infty}^{\infty} F(k) e^{i2\pi kx} dk \tag{3.36}$$

Using the transformation

$$x' = x - \mu_f \tag{3.37}$$

the Fourier transform of $f(x)$ is given by

$$\begin{aligned} F\big(f(x)\big) &= \frac{1}{\sqrt{2\pi}\sigma_f}\int_{-\infty}^{\infty} e^{-\frac{x'^2}{2\sigma_f^2}} e^{-i2\pi k(x'-\mu_f)} dx' \\ &= \frac{e^{-i2\pi k\mu_f}}{\sqrt{2\pi}\sigma_f}\int_{-\infty}^{\infty} e^{-\frac{x'^2}{2\sigma_f^2}} e^{-i2\pi kx'} dx' \end{aligned} \tag{3.38}$$

Using Euler`s formula [57]

$$e^{i\theta} = \cos\theta - i\sin\theta \tag{3.39}$$

the term in $e^{x'}$ can be split to give

$$F\big(f(x)\big) = \frac{e^{-i2\pi k\mu_f}}{\sqrt{2\pi}\sigma_f}\int_{-\infty}^{\infty} e^{-\frac{x'^2}{2\sigma_f^2}} [\cos(2\pi kx') - i\sin(2\pi kx')] dx' \tag{3.40}$$

The term in $\sin(x')$ is odd so its integral over all space is zero, leaving

$$F\big(f(x)\big) = \frac{e^{-i2\pi k\mu_f}}{\sqrt{2\pi}\sigma_f}\int_{-\infty}^{\infty} e^{-\frac{x'^2}{2\sigma_f^2}} \cos(2\pi kx')\, dx' \tag{3.41}$$

This integral is given in standard form as [58]

$$\int_0^{\infty} e^{-at^2}\cos(2xt)\, dt = \frac{1}{2}\sqrt{\frac{\pi}{a}} e^{-\frac{x^2}{a}} \tag{3.42}$$

so

$$F\big(f(x)\big) = e^{-i2\pi k\mu_f} e^{-2\pi^2\sigma_f^2 k^2} \tag{3.43}$$

The Fourier transform of $g(x)$ will give a similar expression, so

$$\begin{aligned} F\big(f(x)\big)F\big(g(x)\big) &= e^{-i2\pi k\mu_f} e^{-2\pi^2\sigma_f^2 k^2} e^{-i2\pi k\mu_g} e^{-2\pi^2\sigma_g^2 k^2} \\ &= e^{-i2\pi k(\mu_f+\mu_g)} e^{-2\pi^2\left(\sigma_f^2+\sigma_g^2\right)k^2} \end{aligned} \tag{3.44}$$

Finally,

$$\begin{aligned} F^{-1}\big[F\big(f(x)\big)F\big(g(x)\big)\big] &= \int_{-\infty}^{\infty} e^{-i2\pi k(\mu_f+\mu_g)} e^{-2\pi^2\left(\sigma_f^2+\sigma_g^2\right)k^2} e^{i2\pi kx}\, dk \\ &= \int_{-\infty}^{\infty} e^{i2\pi k(x-(\mu_f+\mu_g))} e^{-2\pi^2\left(\sigma_f^2+\sigma_g^2\right)k^2}\, dk \end{aligned} \tag{3.45}$$

Applying Euler`s formula again and making the odd integral zero gives

$$F^{-1}\big[F\big(f(x)\big)F\big(g(x)\big)\big] = \int_{-\infty}^{\infty} e^{-2\pi^2\left(\sigma_f^2+\sigma_g^2\right)k^2} \cos\Big(2\pi k\left(x-\left(\mu_f+\mu_g\right)\right)\Big)\, dk \tag{3.46}$$

Using the standard integral in equation (3.42) gives

$$F^{-1}\big[F\big(f(x)\big)F\big(g(x)\big)\big] = \frac{1}{\sqrt{2\pi\left(\sigma_f^2+\sigma_g^2\right)}} e^{-\frac{\left(x-(\mu_f+\mu_g)\right)^2}{2\left(\sigma_f^2+\sigma_g^2\right)}} \tag{3.47}$$

Hence the convolution of the two Gaussian profiles is also a Gaussian with mean equal to the sum of means $\mu_f + \mu_g$, and standard deviation $\sqrt{\sigma_f^2 + \sigma_g^2}$.

Since the width of the spectrum is proportional to the standard deviation of the Gaussian function, the observed spectrum can be suitably fitted to a Gaussian whose width is the quadratic sum of the two contributing Gaussians

$$(\Delta\lambda_{Total})^2 = \left(\Delta\lambda_{Doppler}\right)^2 + (\Delta\lambda_{Instrumental})^2 \tag{3.48}$$

Chapter Four

IDS Components, Alignment and Calibration

4.1 Introduction

In this chapter, the specific details of the IDS system will be described. To begin, a description of the components of the IDS system will be given. Also, the procedures including aligning and calibrating the IDS system will be discussed.

4.2 Mode of Operation

Impurity ions emit radiation during plasma discharges. This radiation is transmitted from the plasma to the spectrometer via an optical fibre. At the spectrometer end, the optical fibre sits just in front of the spectrometer entrance slit. Radiation transmitted through the entrance slit is collimated and directed towards the diffraction grating by a collimating mirror. The parallel beam is then dispersed by the diffraction grating and part of it falls on a focusing mirror, which directs and focuses a spectrum at the exit slit. At the exit of the spectrometer, the spectrum is magnified by a fused silica cylindrical rod lens. The magnified spectrum is then detected by a 16-channel PMT array.

4.3 The Spectrometer

The spectrometer used in the IDS system is the SPEX 1702 manufactured by Spex Industries. A schematic is shown in figure 4.1. The 1702 model is a 0.75 meter spectrometer whose drive is linear in wavelength. It is a plane grating, symmetrical Czerny-Turner spectrometer capable of detecting wavelengths from 0 Å to 15000 Å with 0.1 Å reading accuracy. It has a reflection grating of 1200 grooves/mm and the entrance slit is adjustable up to 3.0 mm with 2 μm minimum divisions. A manual knob on the side is used to rotate the grating to the needed wavelength through the sine bar. The operating principle of the sine bar is illustrated below.

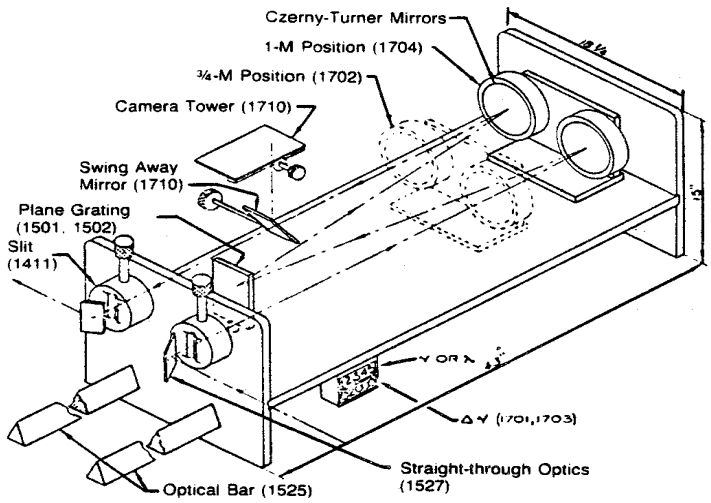

Figure 4.1: Schematic diagram of SPEX 1702 spectrometer [38].

The grating is set up such that the incident and diffracted rays are on the same side of the grating normal. Let the groove separation of the grating be d and let θ_i and θ_d be the angles of incidence and diffraction measured relative to the grating normal. This geometry is shown in

figure 4.2. Consider two rays marked 1 and 2. Ray 1 has two path length differences. First, ray 1 must travel a distance $d\sin(\theta_i)$ further than ray 2 to reach the grating. Then, to reach a point on a line perpendicular to the diffracted rays, ray 1 must travel $d\sin(\theta_d)$. The total path length difference between rays 1 and 2 is thus $d(\sin(\theta_i) + \sin(\theta_d))$. The nth order bright fringe is observed when the total path length difference is an integer multiple of the wavelength of the light being observed. With this geometry, the fundamental grating equation for the nth order bright fringe is given as

$$n\lambda = d(\sin(\theta_i) + \sin(\theta_d)) \tag{4.1}$$

Consider an auxiliary line bisecting the angle formed by the incident and diffracted rays. Denote by θ_c the angle from the bisector to the grating normal. Defining $2\gamma \equiv \theta_d - \theta_i$,

$$\theta_i = \theta_c - \gamma \tag{4.2}$$

$$\theta_d = \theta_c + \gamma \tag{4.3}$$

Substituting these into equation (4.1) gives

$$n\lambda = 2d\sin\theta_i\cos\gamma \tag{4.4}$$

From equation (4.4), there is a linear relationship between $\sin\theta_i$ and $n\lambda$. In effect, adjusting $\sin\theta_i$ can adjust the wavelength to which the spectrometer is tuned. This is the operating principle of the sine bar of the spectrometer which rotates the grating, thus changing $\sin\theta_i$.

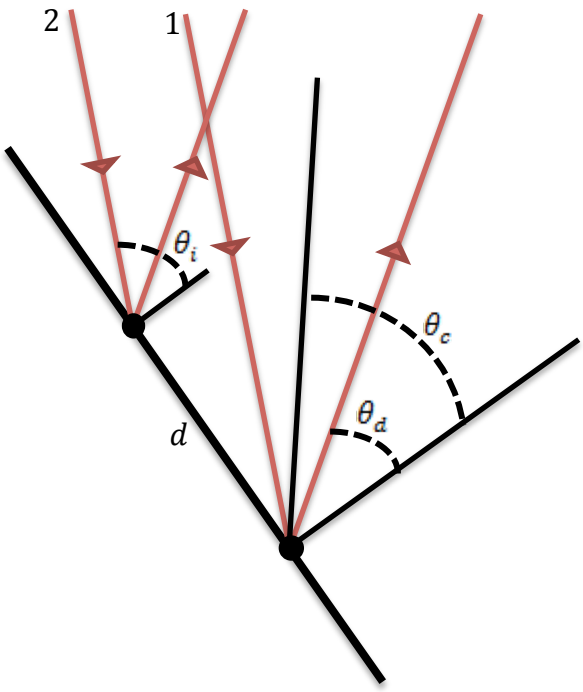

Figure 4.2: Geometry of diffraction. Both the incident and diffracted rays are on the left side of the grating normal.

4.4 Dispersion of the Spectrometer

As explained earlier, the wavelength at which the spectrometer is to observe is specified by the choice of $\sin\theta_i$. However, in practice, the light observed by the spectrometer is not always monochromatic. When light that is not of the wavelength for which the spectrometer is set is incident on the spectrometer, then for the condition that the total path length difference to be an integer multiple of the wavelength, $\sin\theta_d$ must change [59].

Light of wavelength for which the spectrometer is set reflects from the grating and is incident on the focusing mirror parallel to its optical axis. These paraxial rays are then focused to a point. However, rays of slightly different wavelength will be incident on the mirror at a small angle θ from the optical axis. These rays are not focused to a point on the optical axis, rather to a point at a height x from the optical axis. Specifically,

$$x = \theta f \tag{4.5}$$

where f is the focal length of the mirror. As a result, light of a different wavelength than what the instrument is set will show up at a different location governed by equation (4.5). A measure of how much spread in wavelength there is for a given displacement at the focal point of the focusing mirror is dispersion D. Mathematically

$$D = \frac{d\lambda}{dx} \tag{4.6}$$

Substituting in the differential of equations (4.4) and (4.6) using the chain rule gives

$$D = \frac{d \cos \theta_d}{nf} \tag{4.7}$$

The dispersion of the spectrometer improves for large n. The IDS system installed on STOR-M is designed to operate at the first order [28].

Another important factor to consider with the spectrometer is the resolution. The resolution of a spectrometer is affected by the diffraction limit of the grating as well as the effect of finite input slit width. From equation (4.5), the diffraction limit of the grating can be approximated as

$$d\theta = \frac{dx}{f} = \frac{\lambda}{W} \tag{4.8}$$

where W is the width of the diffraction grating. Combining equations (4.8) with (4.6) and (4.7) gives

$$d\theta = dx\frac{d\cos\theta_d}{nf} = \frac{\lambda}{W}\frac{d\cos\theta_d}{n} \tag{4.9}$$

The ruling number N is defined as the width of the diffraction grating divided by the distance between neighboring grooves

$$N = \frac{W}{d} \tag{4.10}$$

For small diffraction angles, $\cos\theta_d \approx 1$ and the diffraction limit of the grating can be simplified as

$$d\lambda = \frac{\lambda}{nN} \tag{4.11}$$

For the IDS system installed on STOR-M, $N = 1200\frac{grooves}{mm}\times 102mm = 1.22\times 10^5\ grooves$. For a typical wavelength of 4000 Å, the resolution due to diffraction is

$$d\lambda = \frac{4000\text{ Å}}{1.22\times 10^5} = 0.033\text{ Å} \tag{4.12}$$

The other factor affecting the resolution of the spectrometer is the effect of the finite input slit width. This effect can be measured quantitatively. The product of the reciprocal linear

dispersion and the input slit width is a measure of this resolution. The spectrometer used in this study was operated at 10 μm input slit width corresponding to a resolution of 0.1 Å.

4.5 Collection and Input Optics

The collection optics consists of a collimating lens connected to a focusing lens via an optical fibre bundle made up of 12 fused silica fibres. Light is collected from a quartz vacuum window on a tangential and normal port at the midplane of the STOR-M chamber. The normal port is used for observing the unshifted wavelength and the tangential port, for the Doppler shifted wavelength. The line of sight of the normal port is in the radial direction while that of the tangential port is tangential to the central line of the tokamak chamber.

Light from the quartz window is focused to the optical bundle by a plano convex lens of diameter 1.0 inch. The fibre bundle at the tokamak end is closely packed, allowing parallel light from the tokamak to be focussed on. At the spectrometer end, the optical fibre is bundled linearly. Light emerging from the spectrometer end of the fibre bundle is collimated by a converging lens to match the entrance slit. A knob located above the entrance is used for adjusting the width of the slit. The input optics at the spectrometer end is mounted on an optical rail allowing its position to be adjusted in order to transmit abundant light. A schematic of the input optics is shown in figure 4.3.

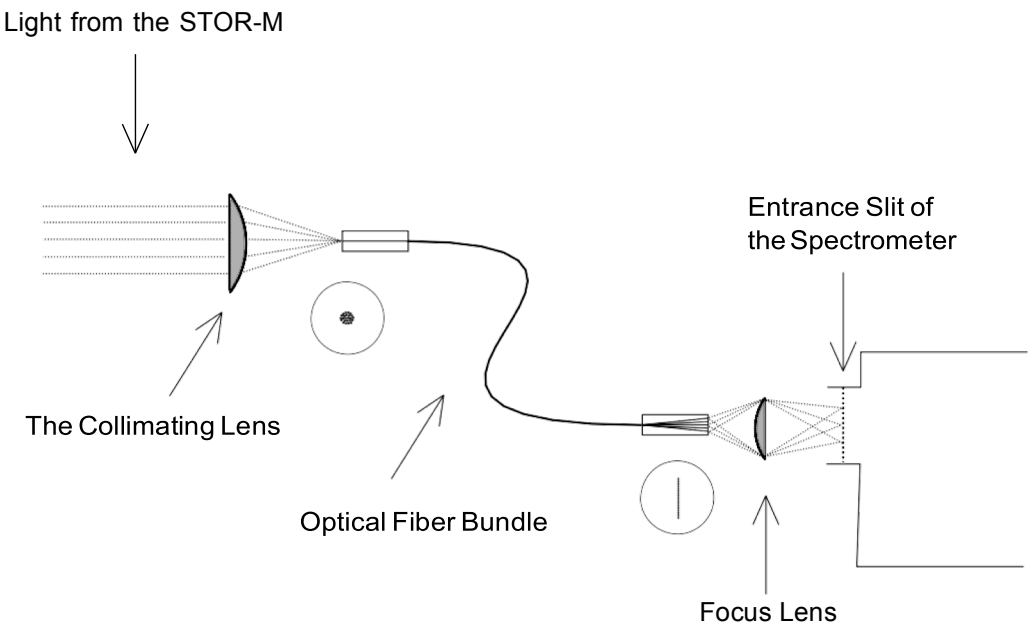

Figure 4.3: Schematic of the light collection optics [28]. It consists of a collimating lens, optical fibre bundle and a focusing lens.

4.6 Exit Optics

The output optics serves to magnify the spectrum in the dispersion direction. The exit optics consists of a fused silica cylindrical rod lens mounted on a stage assembly. The stage assembly is capable of rotating around the optical axis of the spectrometer as well as translating in three dimensions. The physical size of the cylindrical lens is 3.14 mm in diameter, 30.0 mm in length and has a focal length of 2.36 mm. The short focal length of the lens makes it have a large magnification M. In order to accommodate for the cylindrical rod lens and the optical stage holding it, the exit slit of the spectrometer is removed. The magnification of the cylindrical rod

lens used in STOR-M has been calculated to be $M \approx 63.6{\sim}212$, depending on the position of the detector. After magnification, the linear dispersion is modified as

$$\left[\frac{d\lambda}{dx}\right]_{magnified} = M\left[\frac{d\lambda}{dx}\right]_{original} \tag{4.13}$$

4.7 The Detector, Electronics and Data Acquisition

The magnified spectrum is detected by a 16-channel photomultiplier tube array consisting of a photocathode, dynodes and anode. Photons incident on the photocathode of the PMT causes emission of photoelectrons. This further generates secondary emissions of electrons in the dynode and the anode captures the generated current. This is the basic principle that governs the operation of the PMT. The PMT used is able to detect light of wavelength from 1650 Å to 8500 Å. Also the photosensitive material in the photocathode has a high quantum efficiency in the wavelength region 2000 Å to 6500 Å with a peak quantum efficiency at 4200 Å [60]. This makes it ideal for the range of wavelengths for this study. The PMT is embedded in a socket assembly which supplies a D.C voltage of -900 V and transfers the current signal. The PMT array together with the socket assembly is mounted on a two-axis translation stage. This permits the tube to be moved in the dispersive direction to allow for proper optical alignment and along the optical axis for focusing. The exit optics, PMT array and translation stage are all enclosed in a light-tight box with a door at the side for adjusting the optical parts.

The current signal form the PMT array is converted to a voltage signal using a current-voltage preamplifier. The preamplifier is built from 467 operational amplifiers with a pick up

resistance of 1 MΩ. The input and output resistance are also chosen to ensure impedance matching with the coaxial cable used to convey the voltage signals to the data acquisition system (DAQ). The schematic of the preamplifier is shown in figure 4.4. The preamplifier is powered by a ± 12 V DC power supply.

The DAQ is equipped with National Instruments NI-6133 digitizers, which have a sampling frequency up to 1 MHz. Signals form the IDS are sampled at 1 MHz after triggering, and the data is recorded by the digitizer for 60 ms. A LabVIEW program is used to interface the digitizer to a computer where the data is stored.

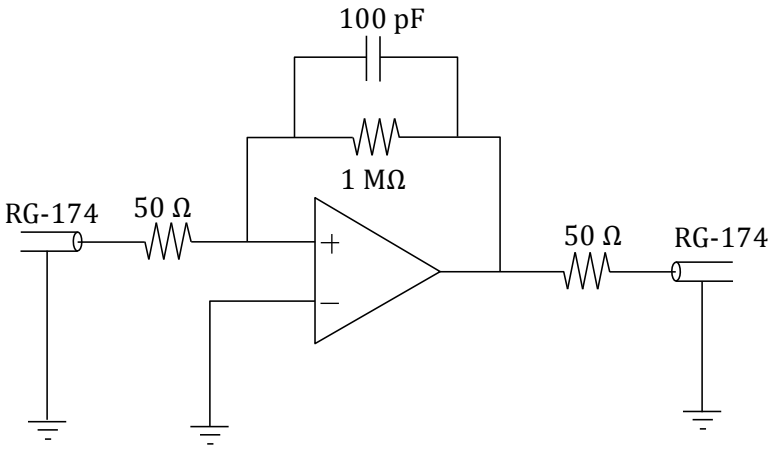

Figure 4.4: Schematic of I-V preamplifier [28]. The combination of the 100 pF capacitor and 1 MΩ resistor works as a low-pass filter with an RC time of 0.1 μs.

4.8 System Alignment and Calibration

For data accuracy, the IDS system has to be aligned and calibrated before measurement. Also calibrating the system enables the dispersion of the IDS to be determined as well as the

absolute wavelength at which a spectral line with zero Doppler shift will appear. The details of alignment and calibration are given below.

To align the system, the bench and the spectrometer is levelled by adjusting the height of the feet using air mounts while observing the bubble for balance. The air mounts minimize mechanical shift of the light spot between two channels by damping the mechanical vibration during plasma discharge. The surface of the PMT is then covered with a piece of white paper and a He-Ne laser of wavelength 6328 Å is used to illuminate the IDS system. The position of the PMT and orientation of the cylindrical rod lens are adjusted until a clear image is seen on the PMT surface. The position of the input optical fibre is also adjusted to ensure the brightest incoming light.

Having aligned the system, the laser is switched off and the sheet of paper is taken off the PMT surface. The IDS system is then calibrated using a mercury lamp. The spectrometer is set to scan over two known wavelengths of the mercury lamp. The wavelengths used are 4358.4 Å and 5460.7 Å. The spectrometer grating motor speed is set to 10 Å/min to scan increasingly over the two wavelengths. Each channel of the PMT records a waveform as the spectrum of the mercury lamp sweeps along the PMT surface. Figure 4.5 shows the calibration waveform obtained. The plot was made using a MATLAB code. The calibration data is sampled for 60 ms after triggering. The plot is smoothened and a relationship between time and the wavelength at which the peak voltage occurs is used to convert time into wavelength. The data is finally fitted to a Gaussian and the parameters are stored on file. From the stored parameters, the area under each Gaussian for the 16 channels is used to calculate the relative sensitivity of the PMT channels. The relative sensitivity result is applied when analyzing data from plasma discharges.

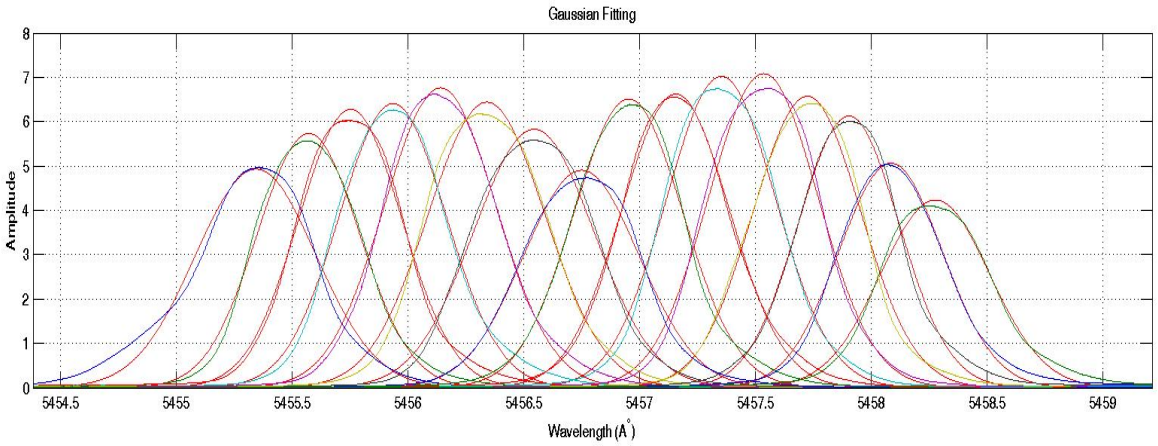

Figure 4.5: Calibration waveform of mercury lamp (blue curves) for each of 16 channels. As the mercury light sweeps across the PMT surface, each channel records a certain waveform. The waveforms are fitted to a Gaussian function (red curves). The fitted Gaussian waveform is superposed on the original waveform.

The difference in peak value of each waveform of the 16 channels can be used to determine the dispersion of the spectrometer. At the present set up, this is found to be about 0.2 Å between two adjacent channels. This result is also applied during data analyses. Other measurements made during calibration include DC offset, instrumental broadening, sensitivity of each PMT channel and wavelength difference between each PMT channel. Table 4.1 summarizes the calibration results. Instrumental broadening can be investigated by observing the spectral waveform of the mercury lamp with varying input slit widths. The broadening is larger as the input slit widens as seen earlier in chapter 3.

Table 4.1: Summary of calibration results.

PMT Channel	Sensitivity of Channel	Width of Gaussian	Wavelength Diff. Between Channels / Å	DC Offset / V
1	1.151	0.648	-1.591	-0.115
2	1.157	0.608	-1.336	-0.108
3	1.115	0.617	-1.161	-0.116
4	1.099	0.613	-0.969	-0.116
5	1.041	0.616	-0.776	-0.129
6	1.040	0.625	-0.581	-0.126
7	1.163	0.634	-0.387	-0.130
8	1.318	0.629	-0.188	-0.131
9	1.089	0.627	0	-0.139
10	1.027	0.633	0.189	-0.129
11	1.058	0.652	0.381	-0.146
12	1	0.651	0.585	-0.142
13	1.028	0.632	0.787	-0.156
14	1.057	0.621	0.982	-0.152
15	1.199	0.625	1.172	-0.138
16	1.310	0.646	1.375	-0.143

Chapter Five

Experimental Results

5.1 Introduction

This chapter focuses mainly on the experimental results obtained from this study. The results of the time resolved flow velocity of impurity ions in STOR-M with the application of both RMP and CTI would be shown. In order to avoid ambiguity in the flow measurements, the definition of the plasma flow direction will be given. Another important point to note is that, the cylindrical rod lens reverses the relative positions of the spectrum and this needs to be factored in when analyzing data.

5.2 Definition of Plasma Flow Direction

The IDS diagnostic installed on the STOR-M tokamak is able to record data with a time resolution of 0.1 ms. This resolution allows fast ion velocity variation investigations in plasma flow measurements. In order to effectively examine plasma flow, a definition of plasma flow direction needs to be established. It is essential to keep a consistent definition through all measurements.

For normal operations in STOR-M, the plasma current is in the counter-clockwise direction while the toroidal magnetic field is in the clockwise direction (all top views). In the reverse current operation mode the plasma current is changed to the clockwise direction and the

toroidal magnetic field direction remains clockwise. To maintain uniformity in the presentation of the flow results, positive flow is defined as counter-clockwise direction (or co-current direction for normal plasma current) whereas negative flow, as clockwise direction. Another important factor to consider during data analyses is the relative position of the PMT channels. The PMT is arranged such that when viewed from the top facing the tokamak, the right side has lower channel numbers. When light from the tokamak enters the spectrometer, the shorter wavelength is diffracted to smaller angle compared with longer wavelength. However, as the diffracted beam exits the spectrometer, the cylindrical rod lens reverses the relative positions of the spectrum. As a result, the lower channel numbers of the PMT record shorter wavelength of the spectrum, which is incorporated in the analyses of the experimental data. The pictorial representation of the setup (top view) is illustrated in figure 5.1.

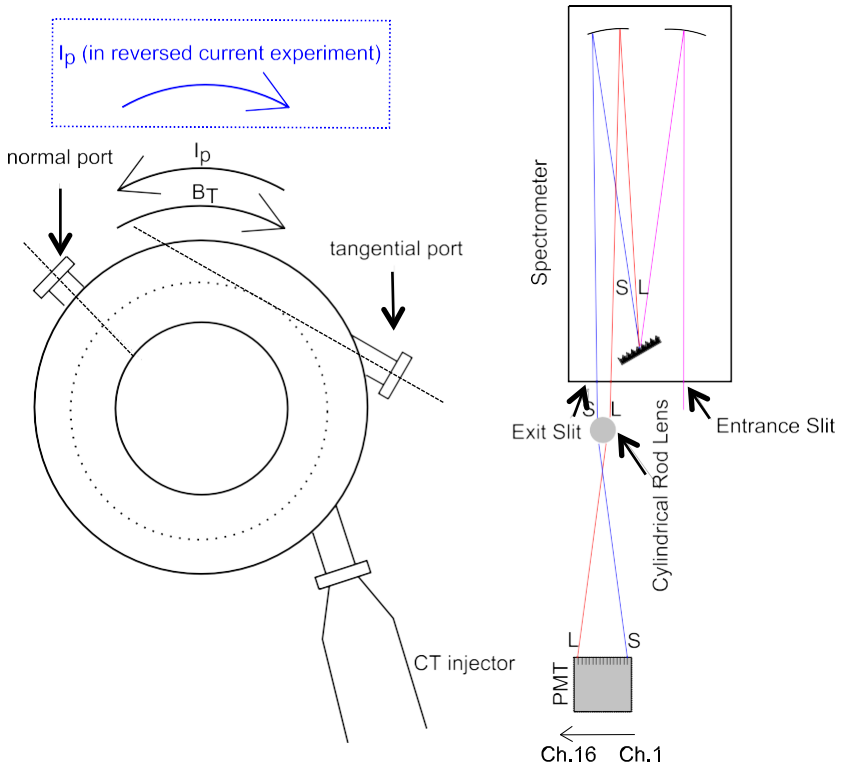

Figure 5.1: Top view of the STOR-M tokamak and the IDS setup [28].

5.3 Plasma Flow with RMP

The effect of the RMP on toroidal plasma flow is examined for different plasma current. Varying the plasma current varies the edge safety factor. Depending on the specific ion species, the plasma current was varied from 10 kA to 22 kA corresponding to a variation in q-value of 3.9 to 9. Varying the voltages to which the slow and fast OH banks were charged varied the plasma current. Generally C_{III} emissions were observable from 10 kA to 22 kA of plasma current whereas O_V and C_{VI}, from 15 kA to 22 kA and 18 kA to 22 kA respectively. In effect, the threshold for emission was observed to be higher for higher ionization states. The plasma discharge parameters were also optimized to avoid disruption during different operations. The toroidal field was kept constant at 0.575 T during the measurement. From the parameters of STOR-M, the edge safety factor $q(a)$ varies with plasma current I_p as

$$q(a) \approx \frac{90}{I_p} \tag{5.1}$$

where I_p is measured in kA. A combination of SRMP and FRMP pulses were applied during the plasma flat top. The RMP pulse was 8 ms long with FRMP fired 3 ms after SRMP as shown in figure 5.1. The pulse was applied 20 ms after OH. During operation with RMP, the chamber pressure was reduced to 9.7×10^{-5} Torr. The RMP current was kept constant during the plasma discharge. Figures 5.3, 5.4, 5.5 and 5.6 show sample traces of STOR-M discharge parameters; plasma current, loop voltage and plasma position (from top), for different plasma current during discharges with RMP.

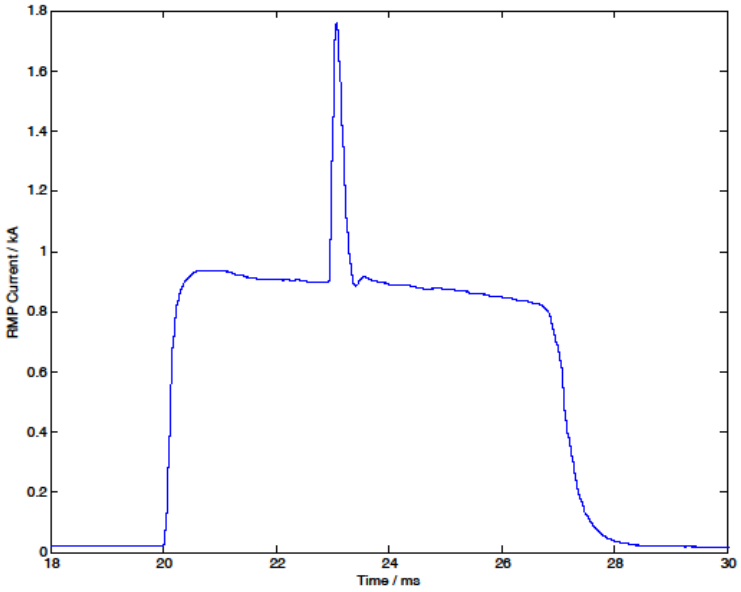

Figure 5.2: Waveform of RMP current. The RMP pulse lasts 8 ms during which FRMP is fired 3 ms after the start of SRMP. The amplitude of the SRMP pulse decays by 120 A during the pulse duration.

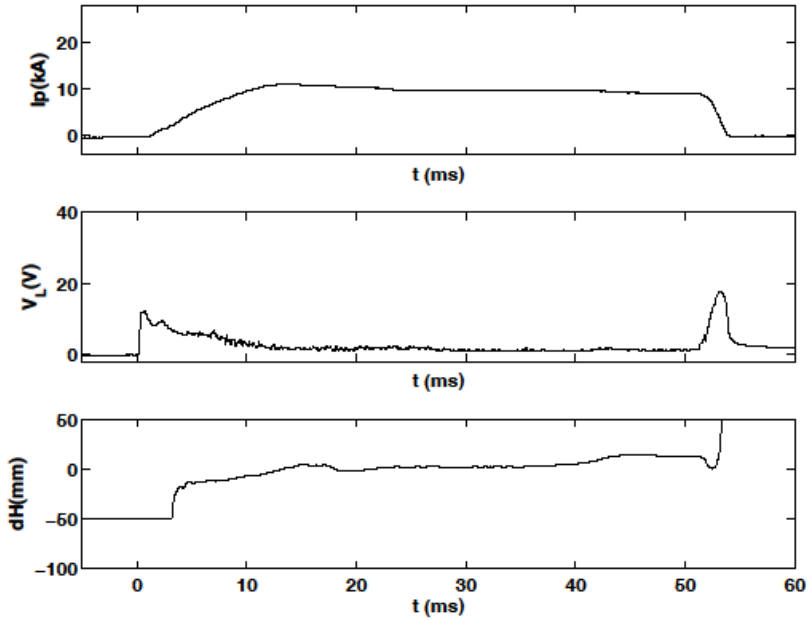

Figure 5.3: Waveforms of plasma current (I_P), loop voltage (V_L) and plasma position (dH) during discharge with RMP. The plasma current is estimated to be 10 kA ($q(a) = 9$).

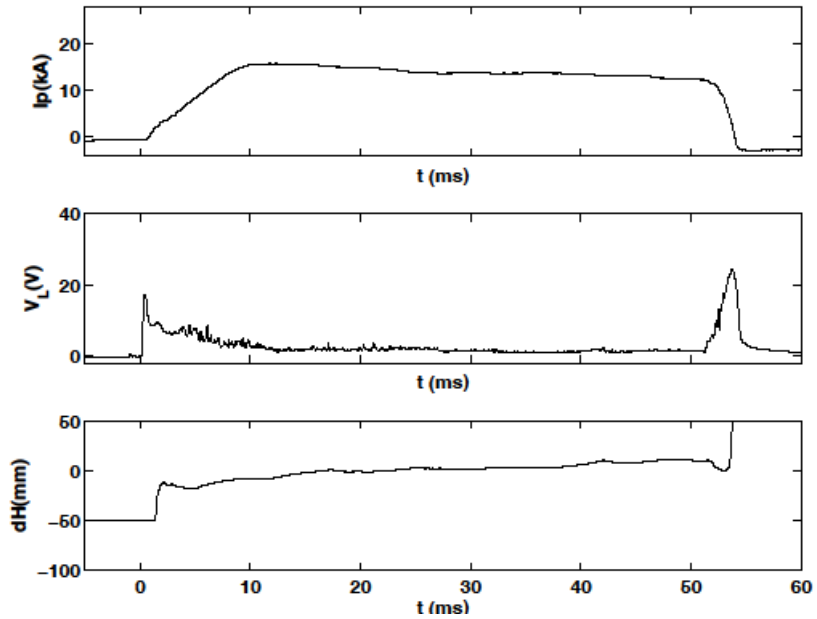

Figure 5.4: Waveforms of plasma current (I_P), loop voltage (V_L) and plasma position (dH) during discharge with RMP. The plasma current is estimated to be 15 kA ($q(a) = 6$).

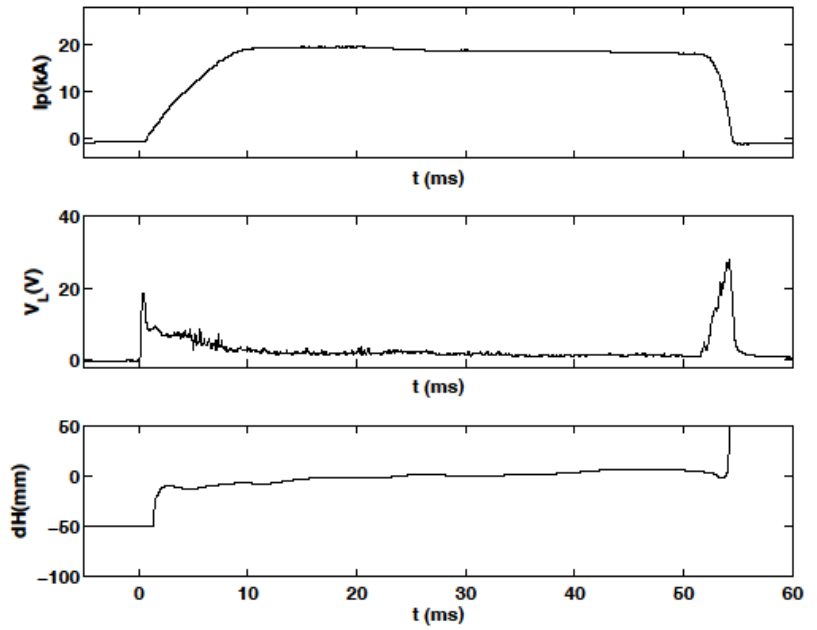

Figure 5.5: Waveforms of plasma current (I_P), loop voltage (V_L) and plasma position (dH) during discharge with RMP. The plasma current is estimated to be 18 kA ($q(a) = 5$).

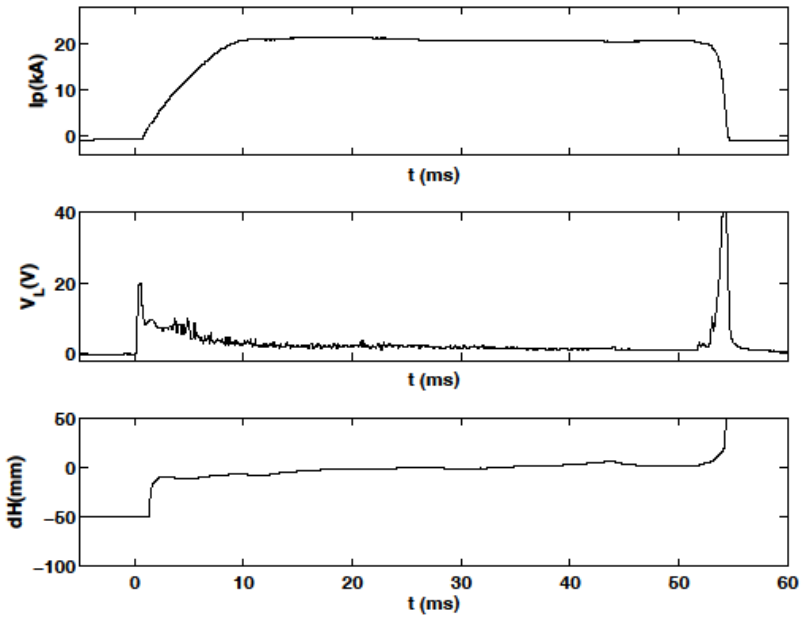

Figure 5.6: Waveforms of plasma current (I_P), loop voltage (V_L) and plasma position (dH) during discharge with RMP. The plasma current is estimated to be 22 kA ($q(a) = 4.1$).

The spectrometer was set to the wavelength of each impurity ion and data from all the diagnostics were collected. The known wavelengths of the impurity ions are 4547.4 Å for C_{III}, 6500.2 Å for O_V and 5290.5 Å for C_{VI}. During the calibration of the IDS system, the offset in the wavelength reading on the spectrometer was measured to be 1.6 Å. Using this difference in wavelength, the wavelength of each impurity ion was adjusted (to correct for the offset) during measurements. As shown earlier, the C_{III} emission line peak is located near $r = 7$ cm, O_V around $r = 3$ cm and C_{VI} line at $r = 0$ cm. Since O_V and C_{VI} emissions occur at the plasma core, they will be referred to as core emissions, whereas C_{III} emission, which occurs at the plasma edge, will be referred to as periphery emission.

For each impurity emission, a normal port viewing radially into the STOR-M chamber was used to observe the unshifted wavelength and a tangential port, for the Doppler shifted

wavelength. Figures 5.7a and 5.7b show the time evolution of C_{III} emission recorded from the normal and tangential port respectively. Each PMT channel records a waveform, making 16 waveforms in total. To analyze the data, all 16 signals measured from both the normal and tangential port at a particular time (λ_i, t for $i = 1{:}\,16$) are fitted to the Gaussian function

$$F(\lambda_i) = A exp\left(-\frac{\lambda_i - \lambda_o}{\sigma}\right)^2 \tag{5.2}$$

where A is the amplitude of the function, λ_i is the calibrated wavelength of the i-th channel, λ_o is the wavelength corresponding to the peak and σ is the width of the Gaussian.

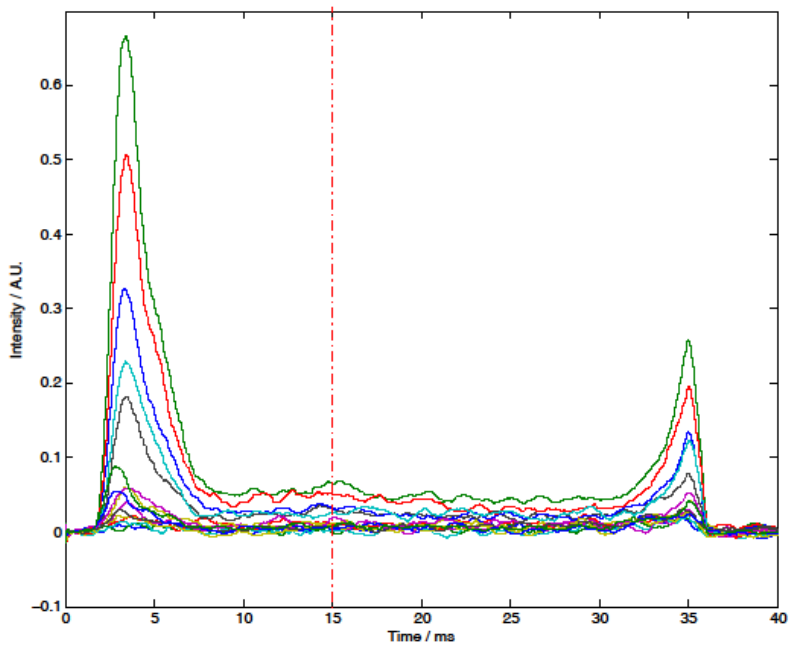

Figure 5.7a: Intensity profile of C_{III} recorded from the normal port during plasma discharge. Data from all 16 channels at a fixed time (say $t = 15$ ms indicated with red dashed line) is fitted to a Gaussian.

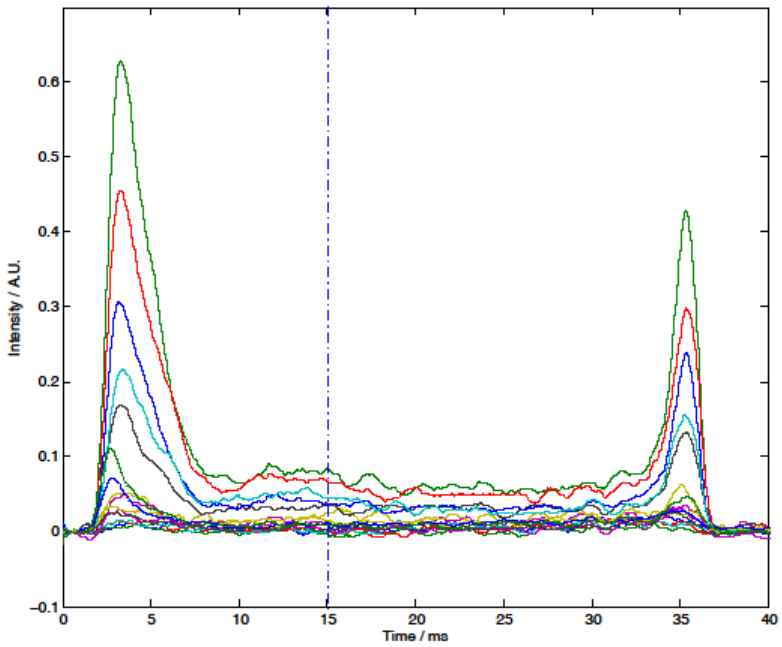

Figure 5.7b: Intensity profile of C_{III} recorded from the tangential port during plasma discharge. Data from all 16 channels at a fixed time (say $t = 15$ ms indicated with blue dashed line) is fitted to a Gaussian.

For each intensity profile shown in figure 5.7, voltage signals from all 16 channels at $t = 15$ ms is plotted in figure 5.8. It can be seen that data from both the normal and tangential port can be modelled by a Gaussian. To evaluate the velocity, voltage signals from all 16 channels (at a fixed time) were fitted to the Gaussian in equation 5.2. Figure 5.9 shows the Gaussian fitted profile for C_{III} for both the normal and tangential reading at $t = 15$ ms. For the tangential reading, it was observed that the peak of the Gaussian profile shifted to larger channel number (and longer wavelength as shown in Fig. 5.1), indicating a red shift for a plasma moving away from the collection lens (counter clockwise or co-current flow). The wavelength difference between each PMT channel was also determined during the system calibration, where channel 9 was taken as the central channel. The wavelength difference between each PMT channel was found to be

about 0.2 Å as shown in table 4.1. This result was applied to each fitted data to convert the PMT channel numbers to wavelengths as shown in figure 5.9. For the plot shown in figure 5.9, the unshifted data (normal port) peaks at 4647.39 Å with FWHM of 2.336, while the shifted data (tangential port) peaks at 4647.51 Å with FWHM of 2.654. The difference between the shifted and unshifted wavelength was used to evaluate the toroidal velocity form equation 3.18 as

$$v = \frac{\Delta\lambda}{\lambda_o} c \tag{5.3}$$

where $\Delta\lambda$ is the difference between the shifted and unshifted wavelength, λ_o is the wavelength of the impurity ion and c is the speed of light. For the C_{III} (at $t = 15$ ms) case shown in figure 5.9, the difference between the peak wavelengths was found to be 0.12 Å which gives a velocity of 8 km/s. Repeating this process for all other values of t, the time evolution of the velocity profile was obtained for the three impurity ions.

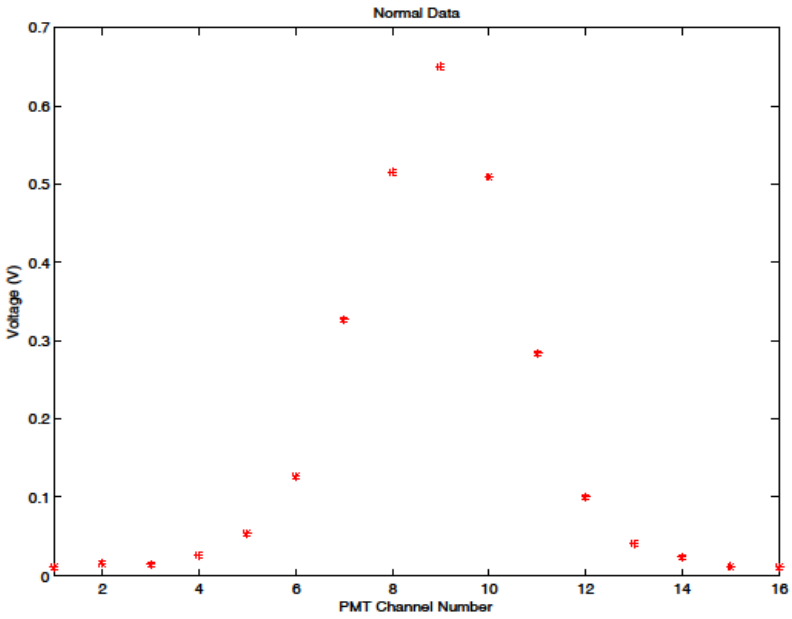

Figure 5.8a: Voltage recorded by the 16 channels of the PMT at $t = 15$ ms from the normal port for C_{III}.

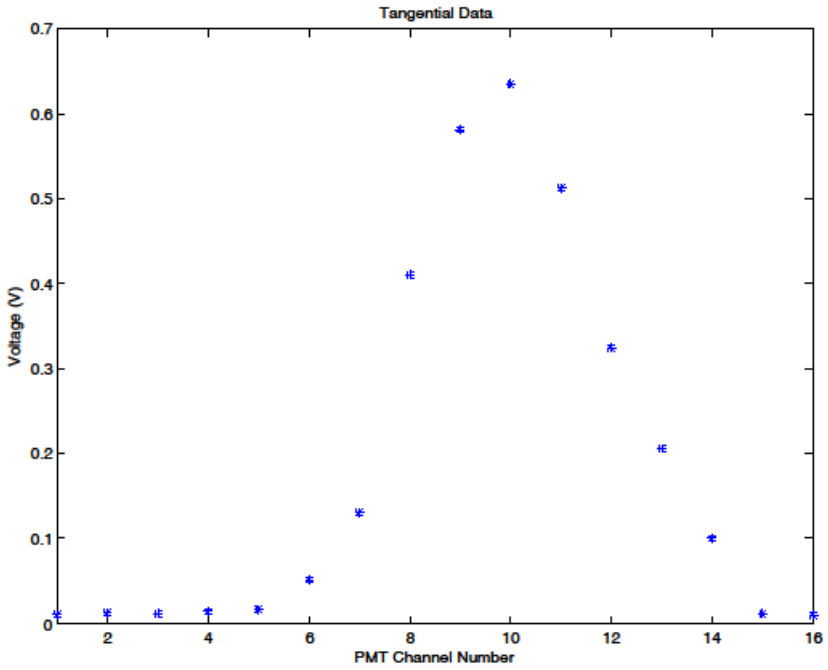

Figure 5.8b: Voltage recorded by the 16 channels of the PMT at $t = 15$ ms from the tangential port for C_{III}.

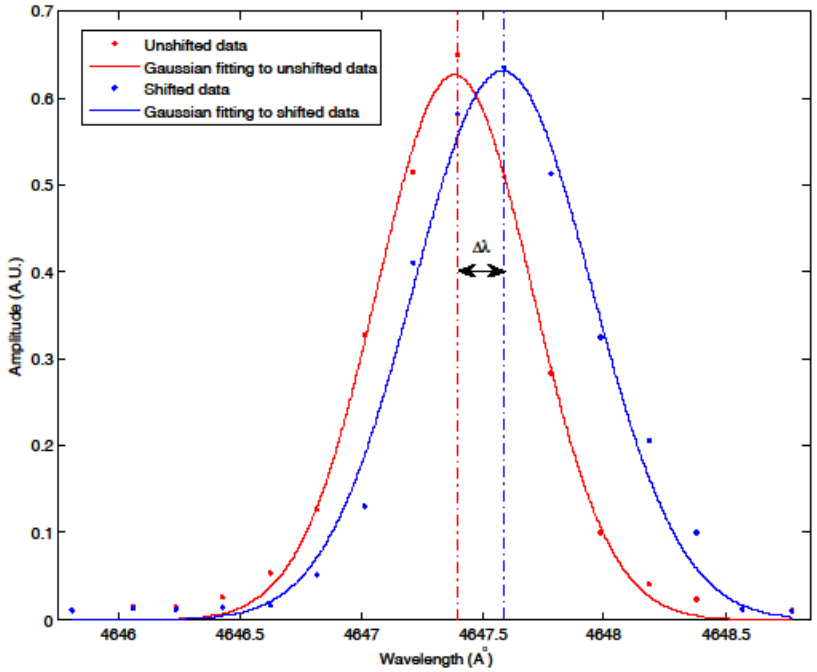

Figure 5.9: Gaussian fitting to data from normal (red) and tangential (blue) port. The calibration data is used to convert the PMT channels to wavelengths with channel 9 chosen as the central channel.

The error in the flow measurements was estimated using the uncertainty in the centroid of the Gaussian fitted peaks for both the shifted and unshifted profiles. For each plasma current, multiple shots were observed. Since the wavelength difference is used in the velocity evaluation, the error in the flow measurement is the sum of the errors in the shifted and unshifed profiles. To avoid clumsiness in the presentation of results, error bars are plotted at 5 ms time interval for each velocity profile. Figures 5.10, 5.12 and 5.13 illustrate the time evolution of the toroidal flow velocity of impurity ions for discharges with RMP. The RMP current profile is superposed above each velocity profile for reference. The flow measurements for both the core and periphery emissions are smoothened for 1 ms. The toroidal flow of C_{III} was measured with both SRMP and FRMP application whereas the core emissions were measured with only SRMP application.

From the result for C_{III}, the base plasma flow velocity is positive, indicating a flow in the counter clockwise direction, or co-current direction. The toroidal velocity is in the range between 4 and 8 km/s at $t = 17$ ms before RMP was applied. The toroidal velocity was observed to increase sharply when RMP was triggered, peaking during both SRMP and FRMP application. The toroidal velocity then reduces gradually to a value below the base velocity after RMP. The peak observed in the velocity profile may be due to additional effects introduced by FRMP pulse. The only way to see the effect of SRMP and FRMP on toroidal flow is to take also, velocity measurements with only SRMP and only FRMP and compare the results. This was however not done in this research.

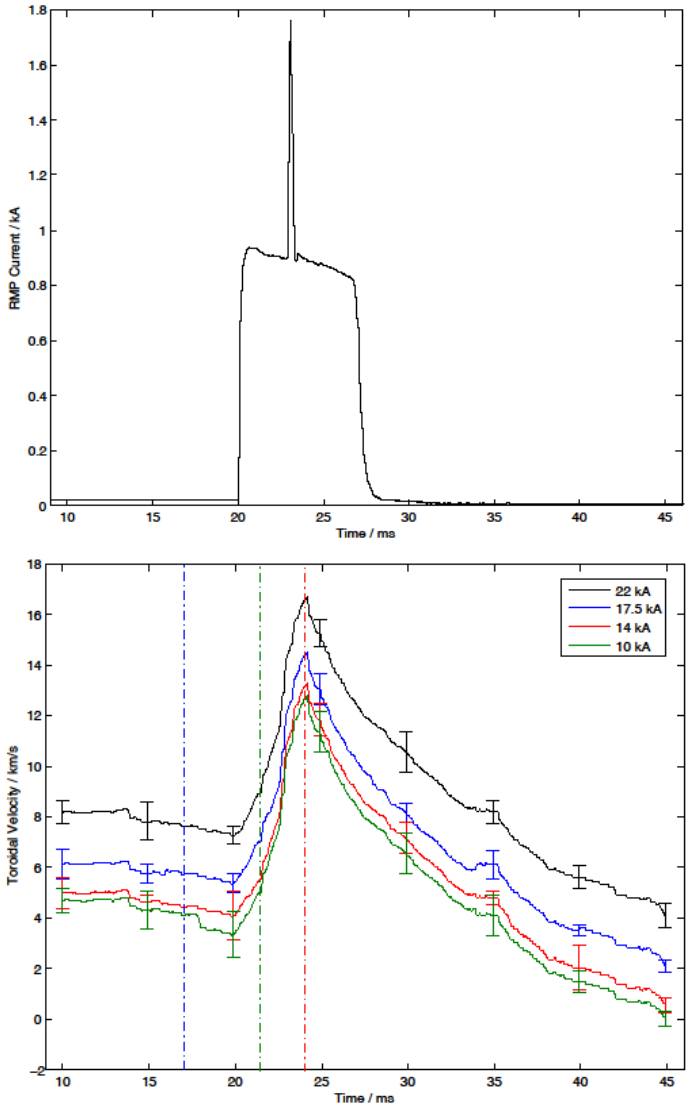

Figure 5.10: Time evolution of the toroidal velocity of C_{III} with RMP profile superposed above. Error bars are plotted at 5 ms time interval and velocities at times indicated by black, red and blue dashed lines would be used to investigate the relationship between plasma current and toroidal velocity.

Figure 5.11 shows the variation of toroidal velocity of C_{III} before RMP at $t = 17$ ms, during SRMP at $t = 21.5$ ms and during the combined SRMP and FRMP pulses at $t = 24$ ms as a function of the plasma current. This plot was created by taking velocity measurements at three specific times (illustrated by dashed vertical lines in figure 5.10) for all plasma current and

plotting them against the plasma current. It was observed that the magnitude of the toroidal velocity increased with plasma current. However a much significant increase was observed when SRMP and FRMP pulses were combined. This may be due to additional factors introduced by the FRMP pulse.

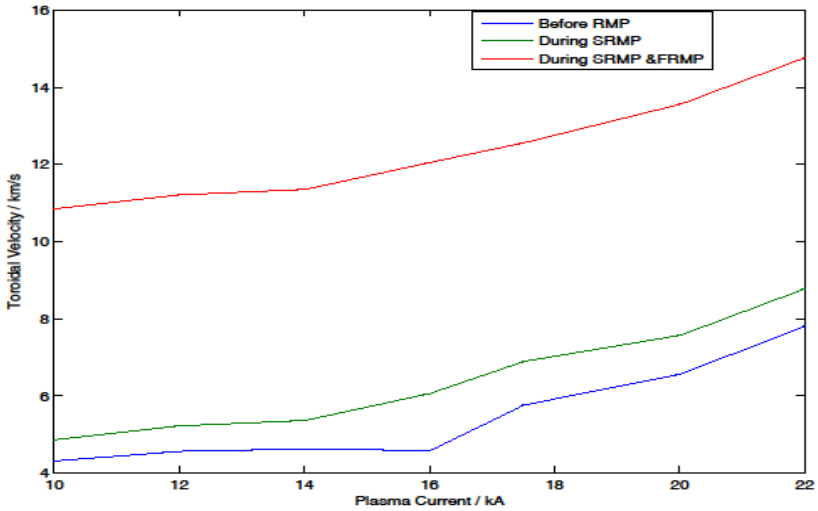

Figure 5.11: Variation in toroidal flow of C_{III} at $t = 17$ ms (before RMP), $t = 21$ ms (during SRMP) and $t = 24$ ms (during SRMP and FRMP) for different plasma current.

Unlike the toroidal flow velocity of C_{III}, the base plasma flow velocity of O_V is negative, indicating a flow in the clockwise direction, or counter-current direction. A steep change in the velocity towards the co-current direction (positive) is observed for about 2 ms when SRMP is applied. The velocity remains fairly constant for the next 5 ms and then reduces sharply to about the base velocity after RMP. The velocity pattern observed for C_{VI} is a little bit different from those of C_{III} and O_V. The toroidal velocity of C_{VI} was observed to increase in absolute value (decrease in magnitude) before SRMP was applied at $t = 20$ ms. The velocity increased further peaking at different times during SRMP. After the SRMP, the toroidal velocity was observed to reduce gradually to a value higher than the base velocity.

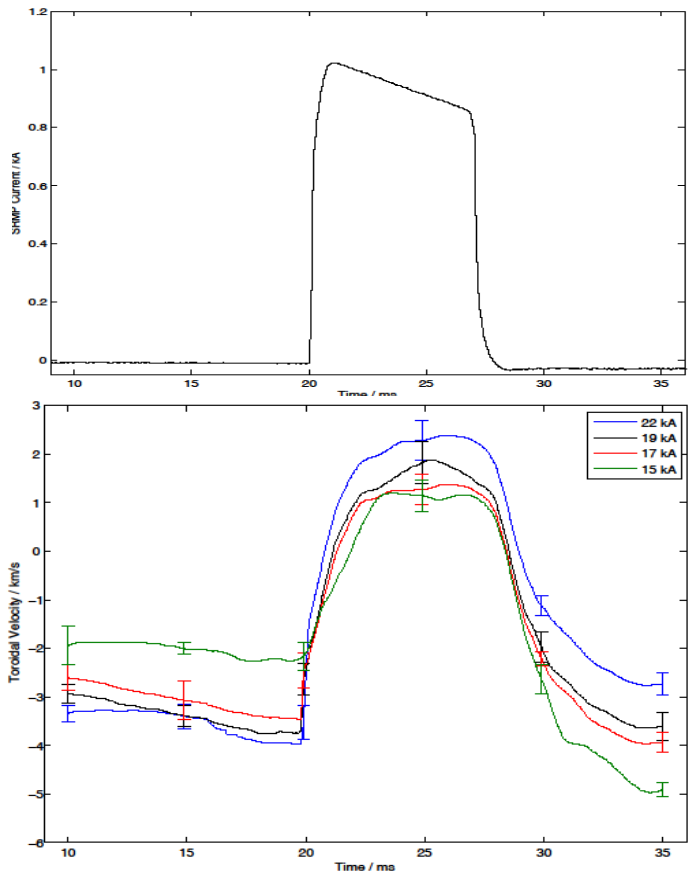

Figure 5.12: Time evolution of the toroidal velocity of O_V with SRMP profile superposed above. The RMP current is almost kept constant at about 1 kA for the different plasma current observed.

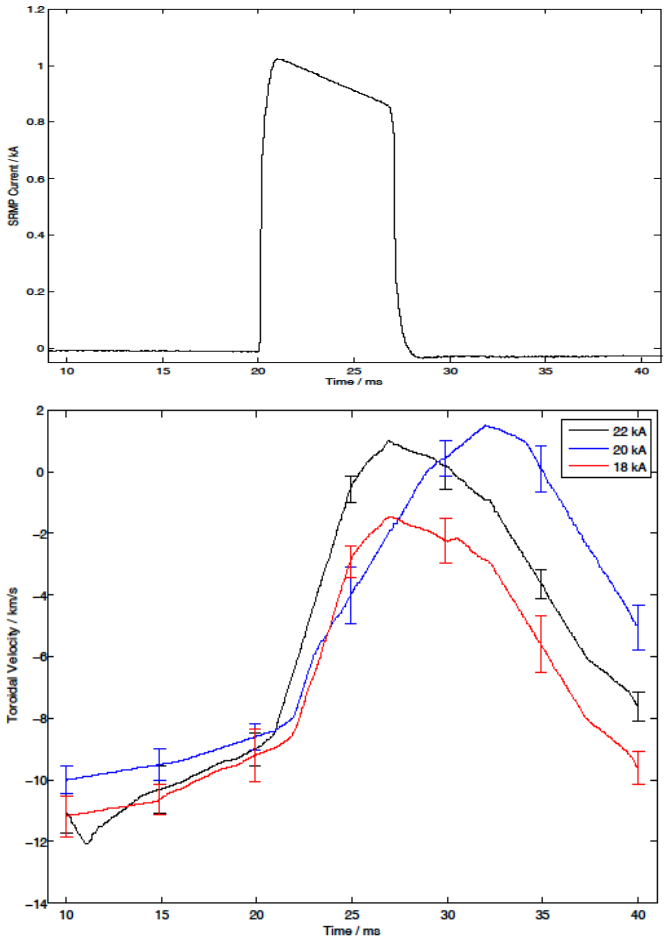

Figure 5.13: Time evolution of the toroidal velocity of C_{VI} with SRMP profile superposed above. The RMP current is almost kept constant at about 1 kA for the different plasma current observed.

For all the three impurity ions, the toroidal velocity of each ion increased in (or towards) the co-current direction when RMP was applied. For C_{III}, there was a further increase towards the co-current direction whereas the core emissions experienced a reversal from the counter current to the co-current direction when RMP was applied. Before SRMP was applied, the toroidal velocities of O_V and C_{VI} were negative, indicating counter-current direction. However on application of the RMP pulse, the toroidal velocities changed and reversed towards the co-current direction. The toroidal velocity of C_{III} increased by about 9 km/s, O_V by about 5 km/s

and C_{VI} by about 9 km/s. The change in toroidal velocity lapsed about 15 ms for C_{III}, 10 ms for O_V and 17 ms for C_{VI}.

Figures 5.14, 5.15 and 5.16 shows the difference in the toroidal velocities of C_{III}, O_V and C_{VI} and their original velocity at $t = 10$ ms as indicated in figures 5.10, 5.12 and 5.13 for plasma discharges with RMP. For C_{III}, the change in the toroidal velocity was relatively small before RMP, increased during the duration of the RMP pulse and maxed out when SRMP and FRMP pulses were combined. Although the base velocity ranged over 3.5 km/s, the effect of RMP on the change in toroidal velocity of C_{III} for the different plasma current shows a similar pattern with only 0.3 km/s (within the error bar) difference in the peak toroidal velocity change.

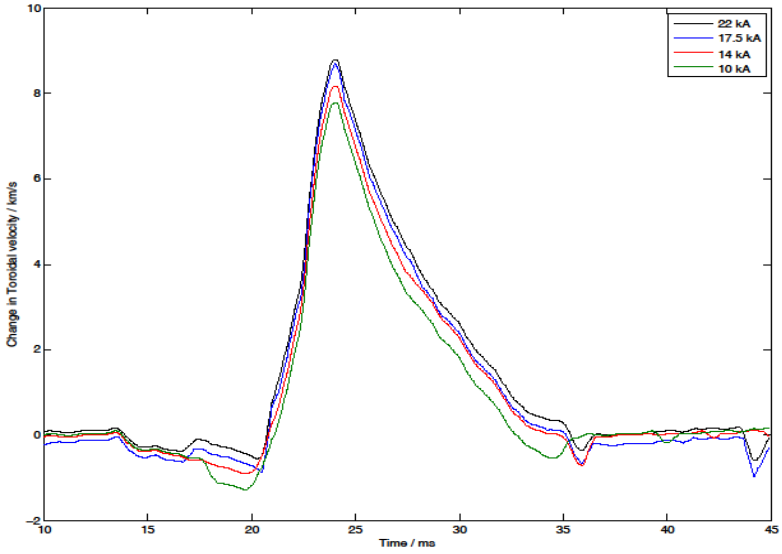

Figure 5.14: Change in toroidal velocity of C_{III} from its original velocity during SRMP and FRMP.

The change in the toroidal velocity of O_V is also relatively small before RMP. During the application of SRMP, the change in toroidal velocity becomes significant for the different plasma current with about 1 km/s difference between each velocity profile during RMP. This may be

due to the $q = 2$ surface being located within the O_V emission location for higher plasma current. The RMP coils on STOR-M are designed to target the $q = 2$ surface. This may have led to the significant change in the toroidal velocity at this location.

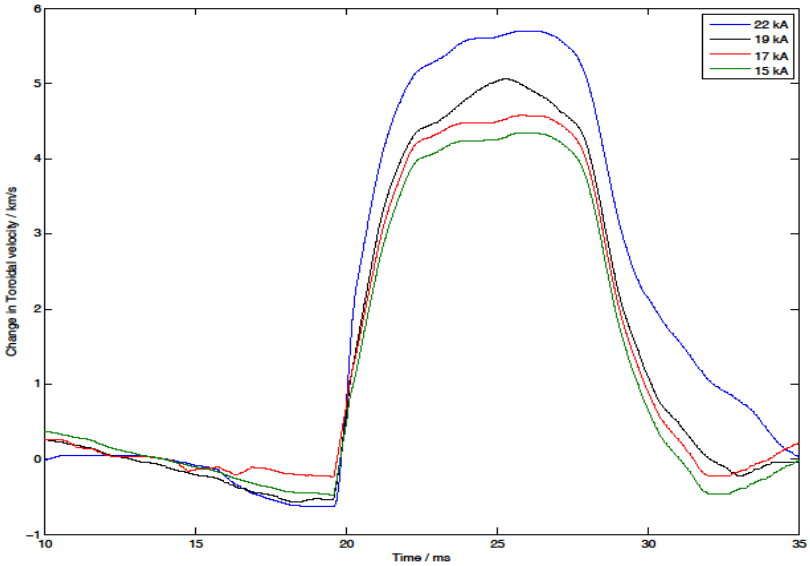

Figure 5.15: Change in toroidal velocity of O_V from its original velocity during SRMP.

The change in the toroidal velocity of C_{VI} like the other two ions is relatively small before RMP and becomes significant during application of SRMP. Unlike the previous cases of C_{III} and O_V, the change in the toroidal velocity assumes different patterns for different plasma current, peaking at different times during SRMP application. Similar to O_V however, the difference in toroidal velocity between plasma current is significant. This can also be attributed to the $q = 2$ surface being located within the C_{VI} emission location as was observed for O_V.

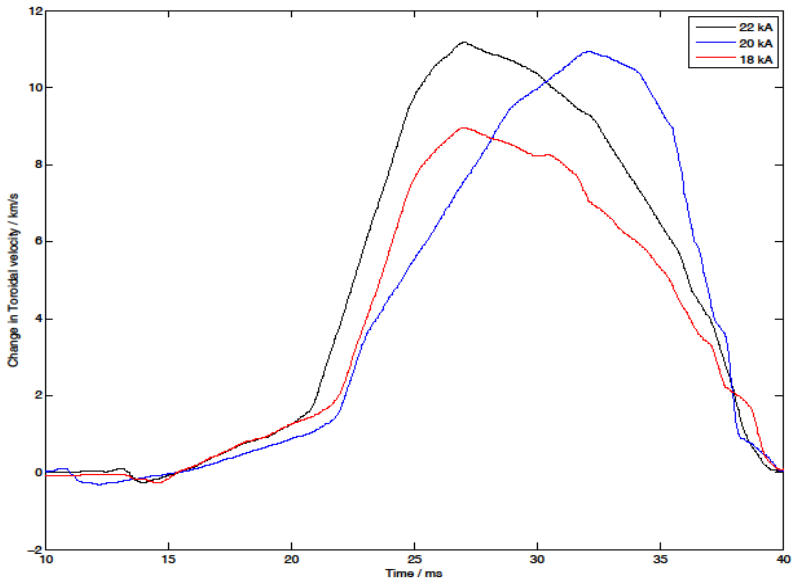

Figure 5.16: Change in toroidal velocity of C_{VI} from its original velocity during SRMP.

Figure 5.17 shows the velocity trace for the impurity emissions for a specific case when $I_p = 22$ kA ($q(a) = 4.1$). For the C_{III} emission, FRMP was triggered 3 ms after SRMP. However, for the core emissions, only SRMP was applied. It is observed that for the same plasma current, the outer and inner impurity ions (C_{III} and C_{VI}) have a higher toroidal velocity compared with O_V (median impurity ion) before RMP. On application of RMP, C_{III} and O_V attain maximum velocity change in a relatively shorter time period compared with C_{VI}. The effect of RMP on the toroidal velocity of the two outer impurity ions (C_{III} and O_V) also diminishes immediately after the RMP pulse is removed. However, the effect of RMP on the toroidal velocity of C_{VI} remains significant even after the duration of the RMP pulse. It should be mentioned that discharge duration during the day when C_{III} and C_{VI} were measured, were typically longer than discharges for O_V. The time interval in figure 5.17 is however truncated to 35 ms so as to compare the results for the impurity emissions. Fast responses of O_V to RMP may

indicate that the velocity change due to RMP is most effective on that location and the slow change of the C_{VI} and C_{III} impurity ions may have indicated a momentum propagation from the radial location of O_V inwards to the core and outwards to the edge.

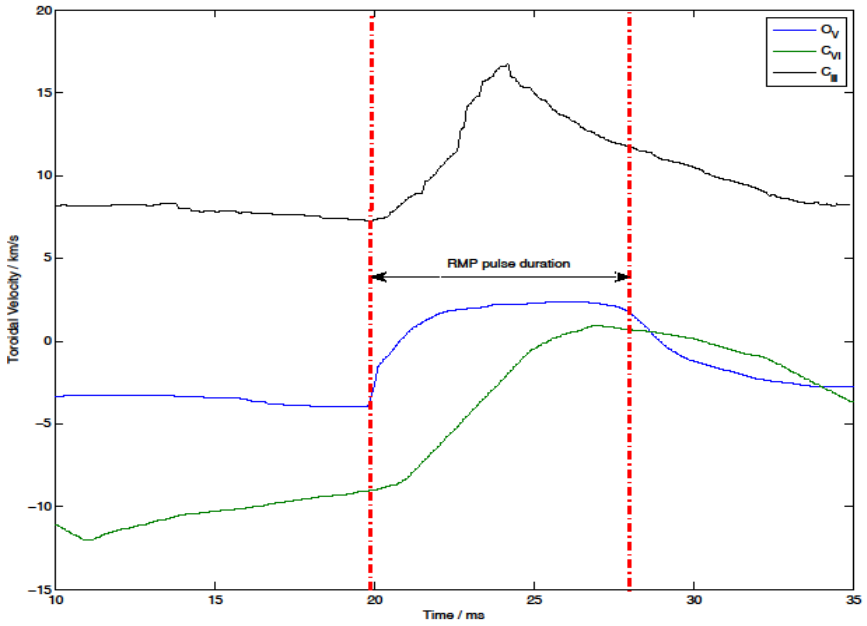

Figure 5.17: Toroidal velocity of the 3 impurity ions during discharge with RMP ($I_p = 22$ kA). The red dashed line is the time during which the RMP pulse is applied.

5.4 Toroidal Flow with Compact Torus Injection

The toroidal flow velocity was also investigated with compact torus (CT) injection. Compact torus has being proposed as a possible fuelling technique for large fusion devices [61]. Compact toroids are self-organized magnetic plasmoids which is formed using coaxial electrodes and a solenoid magnetic field coil. The CT plasmoid, similar to tokamak plasma, has both poloidal and toroidal magnetic fields. A University of Saskatchewan Compact Torus Injector (USCTI) has been installed on the STOR-M tokamak to inject tangentially into STOR-M plasma. The plasmoid can be injected at very high velocities in fast time periods. Typically, the CT penetration is in 10's of microseconds but its effect on the tokamak plasma is lasting. The setup of the CTI is shown in figure 5.18. The injector is attached at the midplane of the tokamak chamber aiming tangentially into the chamber through a port. During injection of CT, the STOR-M discharge parameters were optimized to avoid disruptions. Specifically, the chamber pressure was reduced to about 7.5×10^{-5} Torr to allow for disruption-free discharges. Figures 5.19, 5.20 and 5.21 show traces of STOR-M discharge parameters with CT injection at $t = 17$ ms (indicated by blue dashed lines). It can be seen that CTI does not noticeably change the global discharge parameters shown in the diagrams. However, the density is expected to increase as observed preciously (Unfortunately, the interferometer did not work during this experimental campaign). It was observed that the duration of the plasma discharges were typically shorter compared to discharges with RMP.

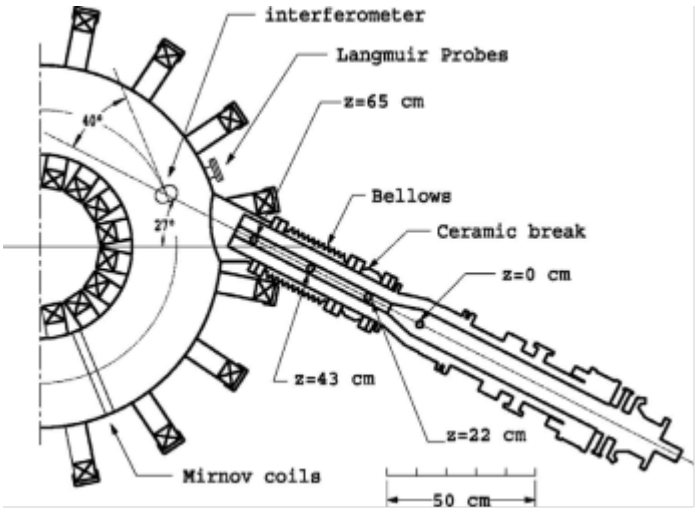

Figure 5.18: Top view of the CTI on STOR-M. The injector is connected to the midplane of STOR-M chamber via bellows.

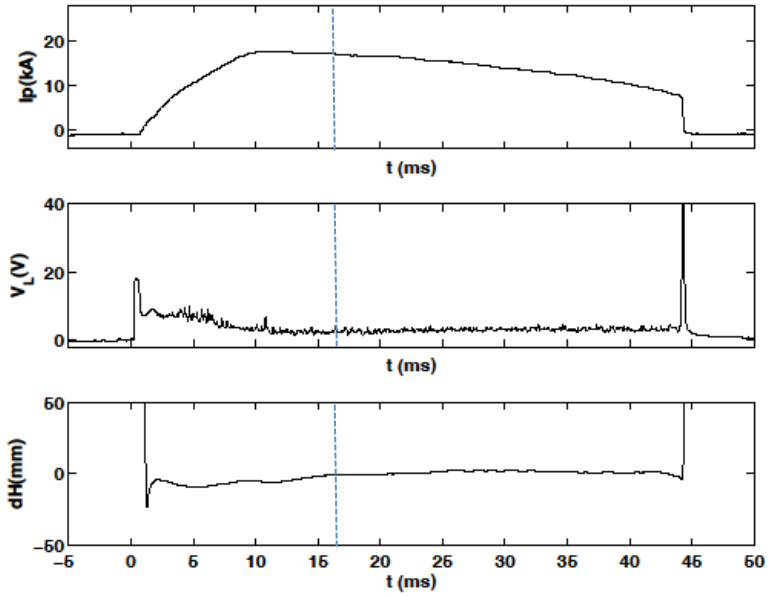

Figure 5.19: Trace of STOR-M parameters during discharges with CT for 15 kA plasma current.

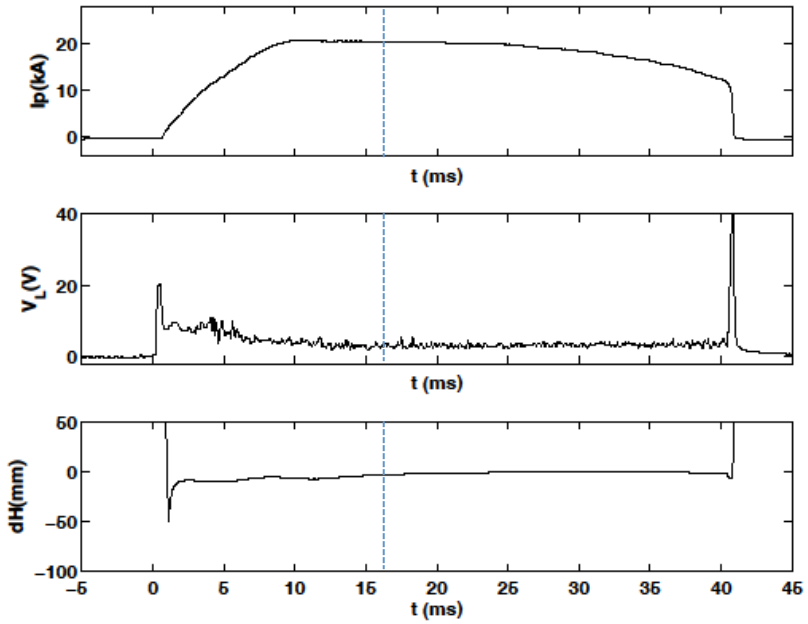

Figure 5.20: Trace of STOR-M parameters during discharges with CT for 18 kA plasma current.

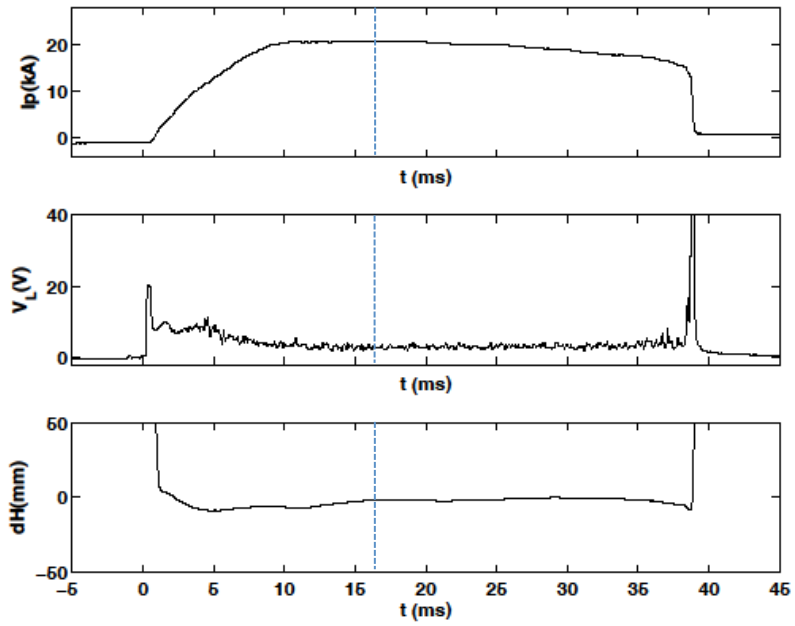

Figure 5.21: Trace of STOR-M parameters during discharges with CT for 20 kA plasma current.

The effect of CT injection on the toroidal flow velocity of STOR-M plasma was investigated for different plasma current. The method of data analyses is the same as was done for the results in Section 5.3. Traces for the flow velocity are smoothened for 1 ms and error bars are plotted for every 5 ms time interval for the velocity traces. Multiple shots were observed for each plasma current with the deviation in each measurement plotted as errors. The results of the flow measurement are shown in figures 5.22, 5.23 and 5.24 for C_{III}, O_V and C_{VI} respectively for a discharge current of 12 kA to 22 kA for C_{III}, 16 kA to 22 kA for O_V and 18 kA to 22 kA for C_{VI}. The CT is set up to inject tangentially in the counter clockwise direction into STOR-M chamber.

The flow velocity of C_{III} was in the co-current direction (same as CTI direction) before CT was triggered at $t = 17$ ms. On injection of CT, the toroidal velocity of C_{III} was enhanced in the CT injection direction. The toroidal velocity was observed to rise sharply (about 1 ms) to a peak value immediately after CT injection. The toroidal velocity reduces sharply and then gradually to a value lower than its initial velocity at the end of the discharge.

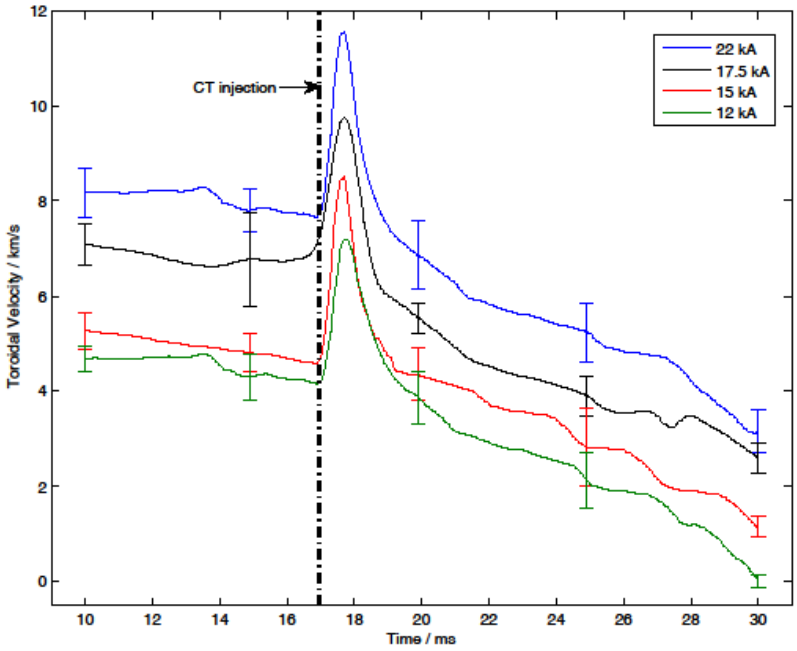

Figure 5.22: Toroidal flow velocity profile of C_{III} during plasma discharge with CT injection. Error bars are plotted for every 5 ms time interval.

The toroidal velocity of the core ions was also modified after CT injection. As shown in figure 5.23, the toroidal velocity of O_V remained fairly constant in the counter current direction before CT injection. The toroidal velocity was observed to increase steeply towards the CT injection direction immediately after CT injection, where it plateaued at the maximum velocity for about 4 ms. It then reduced to a value lower than its initial velocity towards the end of the discharge. However, for $I_p = 22$ kA ($q = 4.1$), the toroidal velocity of O_V dropped 2 ms after reaching its maximum forming a step in the profile. All the same, the profile observed for the different plasma current was similar.

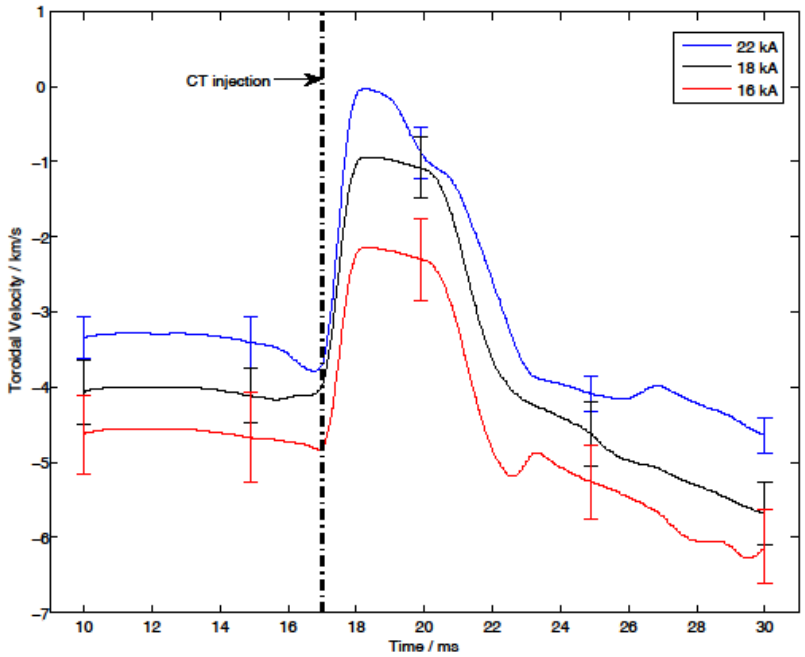

Figure 5.23: Toroidal flow velocity profile of O_V during plasma discharge with CT injection. Error bars are plotted for every 5 ms time interval.

The toroidal velocity of C_{VI} was observed to reduce by about 15% in the counter current direction before CT was triggered. After CT injection, a sharp increase in the toroidal velocity towards the CT injection direction was observed. After reaching a maximum velocity, a slight reduction in the velocity (about 10%), was observed for about 6 ms. This was followed by a steep decrease in the toroidal velocity towards the end of the discharge. Also, for $I_p = 22$ kA ($q = 4.1$), the toroidal velocity reduced after attaining maximum velocity causing a dip in the profile. However, in general, a similar velocity profile was observed for the different plasma current.

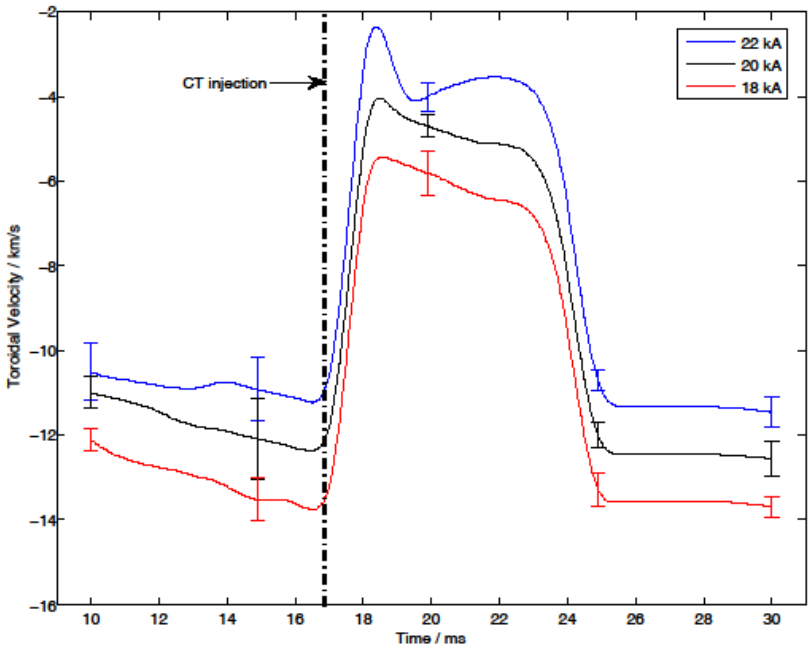

Figure 5.24: Toroidal flow velocity profile of C_{VI} during plasma discharge with CT injection. Error bars are plotted for every 5 ms time interval.

Figure 5.25 compares the toroidal velocity of the three ions for the case when $I_p = 22$ kA ($q = 4.1$). As observed, the toroidal velocity of C_{III} increased by 4 km/s for 2 ms in the same direction as CT injection. That of O_V and C_{VI} also increased by 3 km/s for 5 ms and 6 km/s for 8 ms respectively. It was observed that for all three impurity ions, the toroidal velocity was enhanced in the CT injection direction with larger velocity modification for the core ions. The modification in the toroidal velocity of the three ions may be attributed to momentum being injected into the plasma when CT is injected. In addition, the enhanced flow observed is also indicative of improvement in the plasma confinement by CT.

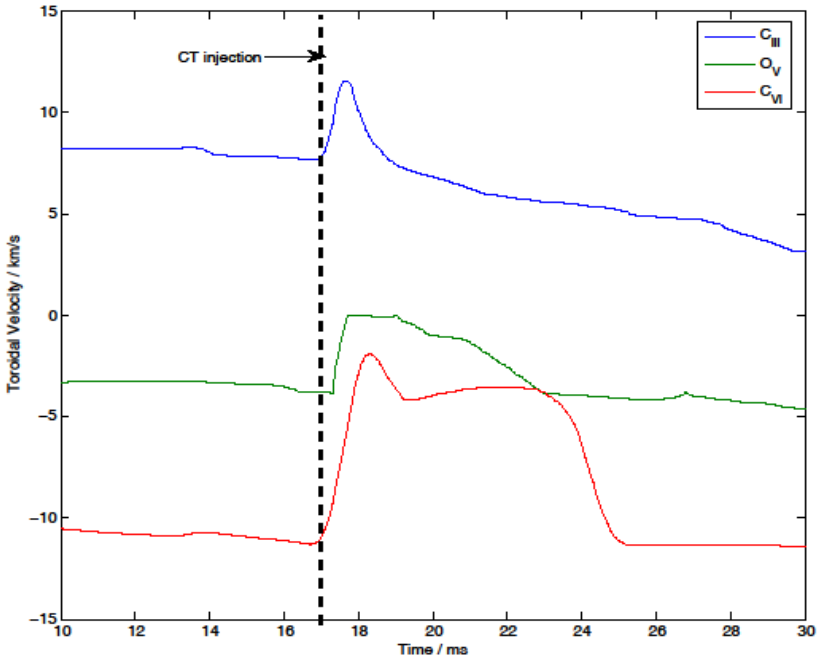

Figure 5.25: Toroidal velocity of the three impurity ions during discharge with CT for the case when $I_p = 22$ kA. The black dashed line indicates the CT injection time.

Figures 5.26, 5.27 and 5.28 show the change in the toroidal flow from its original velocity for C_{III}, O_V and C_{VI} respectively. The change in the toroidal velocity of C_{III} is approximately zero before CT injection. An increase in the toroidal velocity was observed when CT was triggered at $t = 17$ ms, reaching a peak at $t = 18$ ms. Noticeably, the peak velocity observed for the smallest current $I_p = 12$ kA was about 1 km/s less than the peak velocity observed for other values of plasma current.

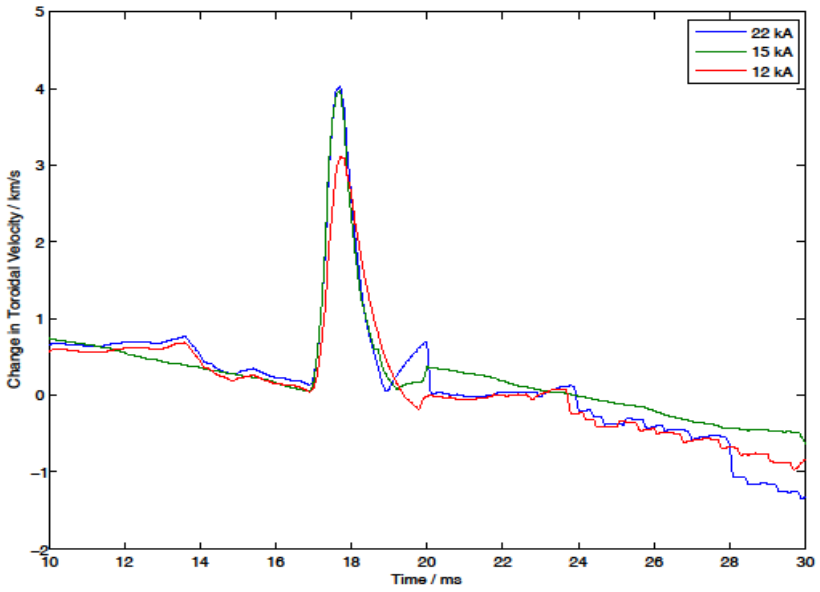

Figure 5.26: Change in toroidal velocity of C_{III} form its initial velocity after CT injection at $t = 17$ ms.

Similarly, the change in the toroidal velocity of O_V was relatively small before CT injection at $t = 17$ ms. After CT injection, a net positive increase in the toroidal velocity was observed for all values of plasma current. The maximum velocity attained and the duration of velocity change was observed to generally increase with increasing plasma current. For all discharges observed with CTI, the toroidal velocity of O_V reduced to a value lower than its base velocity at the end of the discharge because the base velocity without CT injection decreases similarly.

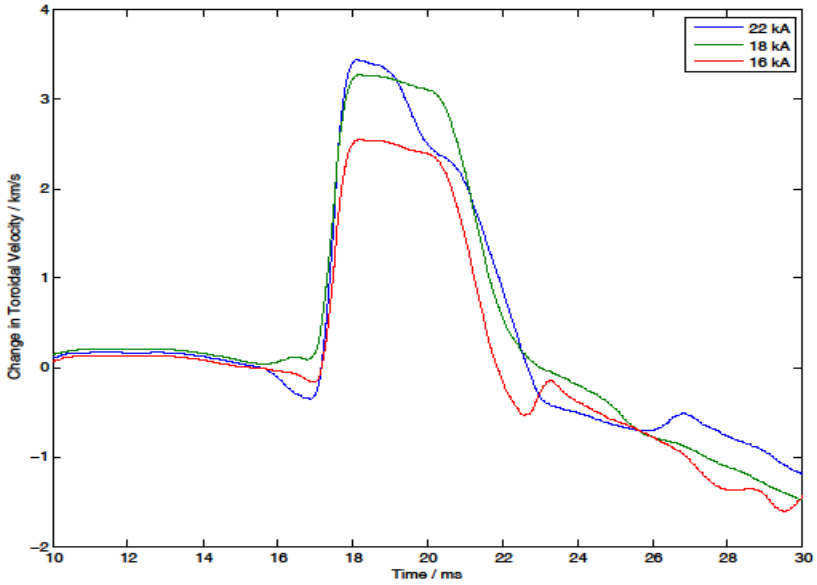

Figure 5.27: Change in toroidal velocity of O_V form its initial velocity after CT injection at $t = 17$ ms.

Although the base velocity for C_{VI} ranges over 2 km/s, the effect of CT injection on the change in the toroidal velocity for different plasma current has a similar profile. However, the profile for $I_p = 22$ kA dips 2 ms after CT injection resulting in a double peak as shown in figure 5.28. Also, for all the plasma current observed, the toroidal velocity reduces back to the base velocity towards the end of the plasma discharge.

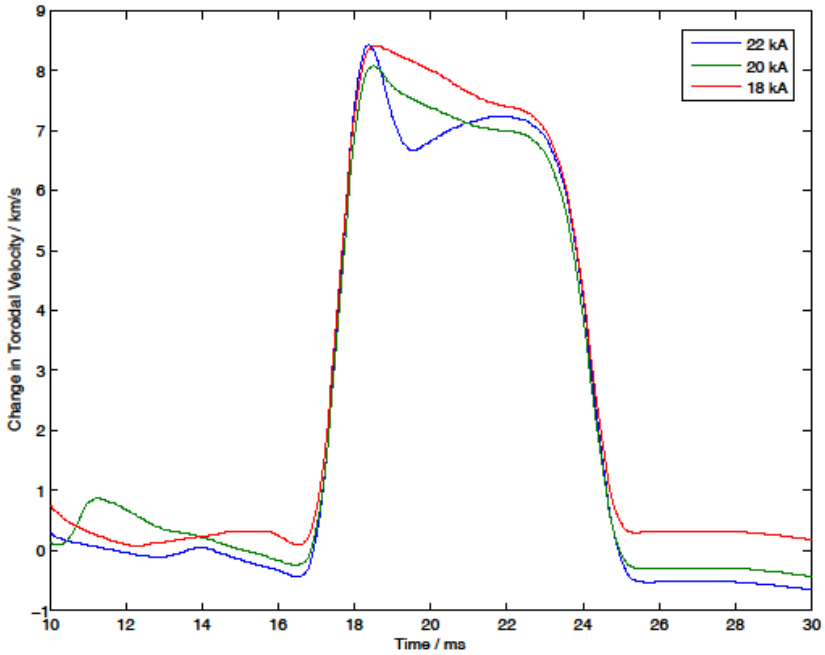

Figure 5.28: Change in toroidal velocity of C_{VI} from its initial velocity after CT injection at $t = 17$ ms.

Chapter Six

Summary and Conclusion

This final chapter of the dissertation will summarize the key results of the research. The IDS system installed on STOR-M has been re-commissioned, calibrated and used to observe spectral line emission from impurity ions during plasma discharges with RMP and CTI. This was done for different edge safety factors corresponding to different plasma current. The time resolved spectral data was used to diagnose the velocity of the edge localized ion emissions and the core ion emissions. Properties of the impurity ions are closely linked to that of the hydrogen ions (main working gas) due to the strong interaction among the ion species. The candidates identified for the flow measurements were C_{III}, O_V and C_{VI}. These ions are intrinsic to STOR-M plasma and no further impurity injection was needed. Ions with lower ionization states are located at the edge of the plasma and those with higher ionization states are located in the core region of the plasma.

The flow velocity was deduced from the unshifted and Doppler shifted wavelength of a specific impurity ion. It was observed that both RMP and CTI have similar effects on the toroidal flow velocity. The velocity of edge ions increased towards the same direction as the plasma current for discharges with both CTI and RMP. However, for the core emissions, the flow is reversed from counter current direction to co-current direction for plasma discharges with RMP and CTI. Typically, the application of RMP caused a longer duration in the change of the plasma velocity compared with that of CTI for the same plasma current since the RMP pulse is much longer than the CT injection time. Also higher plasma current (lower edge safety factor) induced

larger change in the toroidal plasma flow. RMP has a significant impact on the toroidal velocity of impurity ions located near the $q = 2$ surface whereas CT enhances the toroidal velocity of both the core and periphery ions. A possible reason may be the suppression of the magnetic islands at the $q = 2$ surface by the RMP coils and injection of toroidal momentum into STOR-M plasma by CT.

Bibliography

[1] G. H. Miley, H. Towner and N. Ivich, *Fusion cross-sections and reactivities*, University of Illinois Nuclear Engineering Report COO-2218-17, Urbana, Illinois (1974).

[2] T. Kammash, *Fusion reactor physics*, Ann Arbor Science, Ann Arbor, Michigan (1975).

[3] S. Glasstone and R. H. Loveberg*, Controlled thermonuclear reactions*, Van Nostrand, Princeton, New Jersey (1960).

[4] S. Pfalzer, An Introduction to inertial confinement fusion, CRC Press, New York (2006).

[5] R. W. Conn, *Magnetic fusion reactors, Fusion Vol. 1*, Academic Press, New York (1981).

[6] L. A Artsimovitsh, Tokamak devices, *Nuclear Fusion*, **12**, 214 (1972).

[7] J. Gross, *Fusion energy*, Wiley, New York (1984).

[8] P. N. Yushimaniv *et al*., IAEA FEC, Vol 3, p. 307 (1991).

[9] K. Hirl, "Nuclear fusion - status and perspectives." online Booklet, www.ipp.mpg.de/ippcms/eng/pr/publikationen/broschueren/, 2011.

[10] K. Ikeda, *Nucl. Fusion*, **50**, 014002 (2010).

[11] T. Fujita, T. Hatae, T. Ozeki, S. Takeji, H. Shirai, Y. Koida, S. Ishida, S. Ide, Y. Ishii, S. Higasshijima, R. Yoshino and Y. Noyatani*, Nucl. Fusion*, **38**, 207 (1998).

[12] O. Mitarai, H. M. Skarsgard and A. Hirose, Fusionm Technol, **20**, 285 (1991).

[13] S. Sen, C. Xiao, A. Hirose and R. A. Cairns, Phys. Rev. Let. **88**, 185001 (2002).

[14] W. Zhang, C. Xiao, G. D. Conway *et al*., Phys. Fluids B **4**, 3277 (1992).

[15] W. Zhang, C. Xiao and A. Hirose, Phys. Fluids B **5**, 3961 (1993).

[16] A. Hirose, C. Xiao, O. Mitarai, I. Morelli and H. M Skarsgard, *Physics in Canada*, Hiro1, march/April (2006).

[17] J. Wesson, *Tokamaks, 3rd ed.*, Oxford Science Publications, Oxford (2004).

[18] K. Miyamoto, *Plasma Physics and Controlled Nuclear Fusion*, Springer-Verlag (2005).

[19] T. H. Osborne, R. N. Dexter and S.C. Prage, Phys. Rev. Lett. **49**, 734 (1982).

[20] R. J. Buttery, M. De` Benedetti, D. A. Gates *et al*., Nucl. Fusion **39**, 1827 (1999).

[21] G. A Navratil, C. Cates, W. A. Reass *et al.*, Phys. Plasmas, Vol. 5, No. 5, May 1998.

[22] R. Fitzpatrick, Nucl. Fusion **33**, 1049 (1993).

[23] O. Mitarai, S. W. Wolfe, A. Hirose and H. M. Skarsgard, Plasma Phys. Controlled Fusion **27**, 395 (1985).

[24] Plasma Physics and Controlled Nuclear Fusion Research, Vol, p. 323 (1989).

[25] A. Hirose, C. Xiao, O. Mitarai, J. Morelli and H. M. Skarsgard, *STOR-M Tokamak Design and Instrumentation*, Physics in Canada, Vol. 62, No. 2, p. 111-120, March/ April 2006.

[26] O. Mitarai *et al*., *Alternating Current Plasma Operation in the STOR-M Tokamak*, Nucl. Fusion, **36**, 1335 (1996).

[27] S. J. Livingstone, *Experimental Study of Density Fluctuations in the STOR-M Tokamak by small-angle Microwave Scattering*, M.Sc. Thesis, University of Saskatchewan, Saskatoon (2012).

[28] Y. Liu, *Toroidal Flow Velocity Measurement in the STOR-M Tokamak by Ion Doppler Spectroscopy*, M.Sc. Thesis, University of Saskatchewan, Saskatoon (2012).

[29] S. G. Elgriw, Studies of Resonant Magnetic Perturbations in the STOR-M Tokamak, Ph.D. Thesis, University of Saskatchewan, Saskatoon (2013).

[30] S. Elgriw, D. Liu, T. Asai, A. Hirose and C. Xiao, Nucl. Fusion **51**, 113008 (2011).

[31] R. H. Huddlestone and S. L Leonard, *Plasma Diagnostic Techniques*, Academic Press (1965).

[32] I. H. Hutchinson, *Principle of Plasma Diagnostics*, 2nd ed., Cambridge University Press (2002).

[33] J. E. Morelli, *Plasma Position Control in the STOR-M Tokamak: A Fuzzy Logic Approach*, Ph.D. Thesis, University of Saskatchewan, Saskatoon (2003).

[34] M. Enaami-Khonsaari, *Modelling and Control of Plasma Position in the STOR-M Tokamak,* Ph.D. Thesis, University of Saskatchewan, Saskatoon (2003).

[35] S. G. Elgriw, *Investigation of Magnetohydrodynamic Fluctuation Modes in the STOR-M Tokamak*, M.Sc. Thesis, University of Saskatchewan, Saskatoon (2009).

[36] National Instruments, *NI 6132/6133 Specifications*, Texas (2004).

[37] Spex Industries, *1702/1704 Spectrometer*, New York (1985).

[38] I. H. Hutchinson, *Phys. Fluids*, **30**, 3777 (1987).

[39] C. Xiao, K. K. Jain, W. Zhang and A. Hirose, *Phys. Plasmas*, **1** (7), July 1994.

[40] I. H. Hutchinson, *Phys. Rev. A.*, **37**, 4358 (1988).

[41] I. H. Hutchinson, *Phys. Plasmas.*, **9**, 1832 (2002).

[42] A. Dinklage, T. Klinger, G. Marx and L. Schweikhard, *Plasma Physics: Confinement:, Transport and Collective Effect,* Springer, New York (2005).

[43] V. S. Voitsenya, *Role of impurity ions in the impurity influx into the plasma of fusion device*, Soviet Journal Plasma Physics, Vol 15(1), p. 6-13 (1989).

[44] P. G. Carolan and V. A. Poittrowicz, *Plasma Physics*, **10**, 1065-1086 (1983).

[45] F. F. Chen*, Introduction to Plasma Physics and Controlled Fusion*, 2nd ed., Plenum Press (1984).

[46] S. Rauf, A. Balakrishna, Z. Chen and K. Collins, J. Appl. Phys., **111**, 023306 (2012).

[47] A. B. Hussam and R. M. Kulsrud, Phys. Fluids **21**, 2271 (1978).

[48] D. Pfirsch and A. Schluter, Report MPI/PA/7/62, Max-Planck-Institut (1962).

[49] A. Thorne, U. Litzen and S. Johansson, *Spectrophysics*, Springer-Verlag, Berlin (1999).

[50] H. R. Griem, *Principles of Plasma Spectroscopy*, Cambridge University Press, Cambridge (1997).

[51] M. Weissbluth, *Atoms and Molecules*, Academic Press, New York (1978).

[52] T. Fujimoto, *Plasma Spectroscopy*, Clarendon Press, Oxford (2004).

[53] D. Salzmann, *Atomic Physics in Hot Plasmas*, Oxford University Press, Oxford (1998).

[54] H. R Griem, *Spectral Line Broadening by Plasmas*, Academic Press (Pure and Applied Physics), London (1974).

[55] I. Hutchinson, *Principles of Plasma Diagnostics*, Cambridge University Press, Cambridge (1994).

[56] H. J. Pain, *The Physics of Vibrations and Waves*, 6th ed., Wiley, Sussex (2005).

[57] L. Euler, *Elements of Algebra*, 3rd ed., Longman, London (1899).

[58] A. Jeffrey and H. H. Dai, *Handbook of Mathematical Formulas and Integrals*, 4th ed., Academic Press, New York (2008).

[59] E. G. Loewen and E. Popov, *Diffraction Gratings and Applications*, Marcel Dekker, New York (1997).

[60] Hamamatsu Photonics, *Photomultiplier Tubes: Basics and Applications*, 3rd ed., Japan (2007).

[61] P. B. Parks, *Phys. Rev. Let.*, **61**(12), 1364-1367 (1988).